S Schmuck et al.

Electron cyclotron emission spectra in X- and O-mode polarisation at JET: Martin-Puplett interferometer, absolute calibration, revised uncertainties, inboard/outboard temperature profile and wall properties

Electron cyclotron emission spectra in X- and O-mode polarisation at JET: Martin-Puplett interferometer, absolute calibration, revised uncertainties, inboard/outboard temperature profile and wall properties

S. Schmuck,[1, a)] J. Fessey,[1] J.E. Boom,[2] L. Meneses,[3] P. Abreu,[3] E. Belonohy,[2] and I. Lupelli[1]

[1)] *CCFE, Culham Science Centre, Abingdon, OX14 3DB, UK*
[2)] *Max-Planck-Institut für Plasmaphysik, Boltzmannstrae 2, D-85748 Garching, DE*
[3)] *Instituto de Plasmas e Fusão Nuclear, Instituto Superior Técnico, Universidade de Lisboa, PT*

At the tokamak JET the electron cyclotron emission spectra in O-mode and X-mode polarisation are diagnosed simultaneous in absolute terms for several harmonics with two Martin-Puplett interferometers. From the second harmonic range in X-mode polarisation the electron temperature profile can be deduced for the outboard side (low magnetic field strength) of JET but only for some parts of the inboard side (high magnetic field strength). This spatial restriction can be bypassed, if a cutoff is not present inside the plasma for O-mode waves in the first harmonic range. Then, from this spectral domain, the profile on the entire inboard side is accessible. The profile determination relies on the new absolute and independent calibration for both interferometers. During the calibration procedure the antenna pattern was investigated as well, and, potentially, an increase in the diagnostic responsivity of about 5% was found for the domain 100–300 GHz. This increase and other uncertainty sources are taken into account in the thorough revision of the uncertainty for the diagnostic absolute calibration. The uncertainty deduced and the convolution inherent for Fourier spectroscopy diagnostics have implications for the temperature profile inferred. Having probed the ECE spectra in opposite polarisation directions for the first harmonic range, a condition is derived for the reflection and polarisation-scrambling coefficients of the first wall on the outboard side of JET.

I. INTRODUCTION

The plasma medium exploited by fusion experiments with magnetic confinement emits broadband spectra. In the microwave and far-infrared spectral domain the electron cyclotron emission (ECE) spectra in X- and O-mode polarisation are emitted by plasma electrons. In general, the ECE spectra carry information about the electron distribution function $f_e(\vec{v}, \vec{r})$ defined for the six-dimensional phase space. More precisely, each polarisation direction and each harmonic range are connected to different domains in that phase space. Standard ECE diagnostic applications probe the second harmonic range in X-mode polarisation (X2) from the low-magnetic field side (outboard side for a tokamak) to characterise the local electron temperature T_e[1–3]. This spectral domain is closely linked with the thermal part of f_e, when the local electron density $n_e = \int f_e d\vec{v}$, and, thus, the optical thickness are large enough. In addition, the large optical thickness for a particular frequency allows the localisation of the corresponding emission layer inside the plasma. As a consequence, the T_e profile is accessible.

At the Joint European Torus (JET) the ECE spectrum is probed mainly in X-mode polarisation for several harmonics in absolute terms with a Martin-Puplett interferometer[4], hereafter referred to as MIX[5–12], from the outboard side. From the second harmonic range (100-250 GHz), for which the plasma is usually optically

thick, information about T_e is extracted. Due to the magnetic field topology, an overlap with the third harmonic range exists which prevents the derivation of T_e for most of the inboard side. Because no or little overlap is present for the first and second harmonic range, T_e can be extracted theoretically from the ECE spectrum of the first harmonic range 50-150 GHz in O-mode polarisation (O1). This has been demonstrated at JET at the proof of principle level[13], relying on simulations with the ECE ray-tracing tool SPECE[14] and measurements with another ECE diagnostic: the heterodyne radiometer[15]. To overcome the impracticalities of this approach, a second Martin-Puplett interferometer (MIO) is used as a basis to probe the ECE spectrum mainly in O-mode polarisation. Indeed, if the cutoff (too high n_e) is not present for the O1 domain, T_e can be derived for the inboard side of JET. Besides this application, a more fundamental topic can be addressed. Any probed polarisation direction has, according to Malus' law, finite contributions of the X- and O-mode polarisation directions. Hence, probing perpendicular polarisation directions allows the quantification of the fractions of the ECE spectra in X- and O-mode polarisation relying on measurements and not on assumptions. For suited conditions this quantification can be achieved with MIX and MIO at JET.

Both interferometers were calibrated absolutely but independently in 2015. However, this calibration has two main issues. Firstly, since the pattern of the in-vessel antenna connected to the transmission line is not known, filling the pattern with the calibration sources is not guaranteed. Secondly, the temporal evolution of the diagnostic sensitivity remains untracked during the years be-
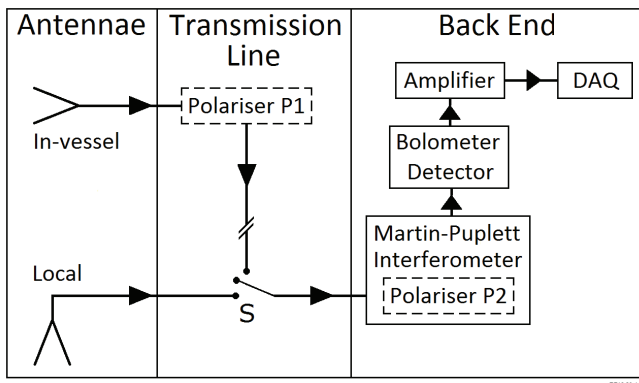
a)Stefan.Schmuck@ukaea.uk

FIG. 1. Scheme for interferometer diagnostics MIX and MIO at JET with major segments: antennae, transmission line and back end. Via the switch S the diagnostic back end is connected to the transmission line either towards the in-vessel or the local antenna. The back end comprises the Martin-Puplett interferometer unit, the bolometer detector, the amplifier stage, and the data acquisition system (DAQ). For plasma operation and calibration the same DAQ is used. The polariser P1 located just outside the JET vessel allows the manual choice of the polarisation direction to be transmitted. To increase the diagnostic sensitivity the wires of the polariser P2, which implements the two input ports of the interferometer, have a parallel orientation with respect to the wires of P1 when followed along the transmission line.
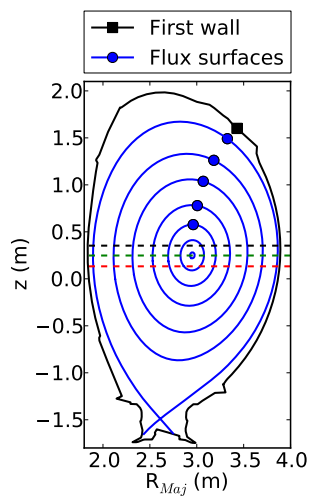

FIG. 2. Lines of sight in vacuum (dashed) for ECE diagnostics (interferometers MIX and MIO and heterodyne radiometer HR) at JET. The apertures of the diagnostic antennae are located behind the first wall of JET at the major radius $R_{Maj} = 4.126$ m in the same poloidal cross-section but at different heights z: 0.133 m for MIO, 0.248 m for HR and 0.353 m for MIX. In general, the diagnostics probe the plasma in the centre indicated by the flux surface geometry for the pulse 89074 at the time 2 s.

tween the calibration periods. Those issues and others lead to an uncertainty in the T_e profile measurement.

The diagnostic hardware and calibration set up for both interferometers is updated in Secs. II and III. The reader can find a more detailed description about the hardware and the calibration performed in 2010 in Ref.[12]. The analyses steps for calibration and plasma operation are then presented in detail (see Sec. IV). This includes a thorough revision of the uncertainties for the calibration and its implications on the profile derivation with the standard approach. The conclusion section completes the paper.

II. DIAGNOSTIC DESIGN UPDATES

The two Martin-Puplett interferometer diagnostics MIO and MIX are very similar in construction and follow the scheme shown in Fig. 1. Each diagnostic is equipped with a local and an in-vessel antenna with the associated transmission lines, the back end comprising the interferometer, the bolometer detector, the post-detection amplifier, and the same data acquisition system for both plasma and calibration operation. The main diagnostic parameters, like the spectral resolution $\Delta_f = 3.66$ GHz, temporal resolution $\Delta t \approx 17$ ms, optical path difference increment $\Delta x = 40$ μm are the same for MIX and MIO. The parameters for which the interferometers differ from each other are summarised in Table I.

Both diagnostics probe the plasma centre from the low-

magnetic-field side (see Fig. 2). The lines of sight in vacuum are located in the same poloidal cross-section in octant 7 of the JET vessel. The apertures of the in-vessel antennae are placed at the major radius $R_{Maj} = 4.126$ m at the heights z = 0.133 m and z = 0.353 m for the O- and X-mode channel, respectively.

The wire polariser housed just outside the JET vessel in each transmission line (see P1 in Fig. 1) is adjusted for horizontally/vertically wire orientation to transmit radiation mainly in X-/O-mode polarisation during plasma operation. A second polariser (see P2 in Fig. 1) implements the two input ports for each diagnostic back end. The orienations of the wires of both polarisers are parallel when followed along the transmission line to optimise the throughput.

The grid attenuator, which has been in place in the back end of MIX to prevent non-linear behaviour of the detection system (see component 8 in Fig. 3 in Ref.[12]),

	MIX	MIO
P	X-mode	O-mode
z (m)	0.353	0.133
M_T	tall	normal
l (m)	$\sim$40	$\sim$38
n_E, n_H	4, 8	8, 4
A_C, A_P (dB)	45, 22	51, 30
σ_{10V}, $\sigma_{7.2V}$ (mV)	17.5, 20.4	16.4, 19.6

TABLE I. Differing parameters of Martin-Puplett interferometers MIX and MIO: Polarisation P probed mainly during plasma operation, height z of in-vessel antenna aperture, transmission line (mainly S band waveguide) used in mode M_T, length l of transmission line, numbers n_E and n_H of mitre bends in E and H plane in transmission line, gains A_C and A_P applied during absolute calibration and plasma operation, noise levels σ_{10V} and $\sigma_{7.2V}$ for bias voltages V_{Bias}=10 V and 7.2 V supplied to the detector at amplifier gain of 45 dB.

was removed since JET pulse 83899. This was justified by an estimation of the dependency of the current, flowing through the detection circuit, on the intensity incident on the detector. In general, as long as the current remains constant, the diagnostic response is linear. This is achieved by the additional high-ohmic resistance (164 kΩ) in the detection circuit (see Section II C in Ref.[12]), and the current changes little even when a high-temperature plasma is probed. For example, for a plasma with a central electron temperature of 10 keV and the bias voltage $V_{Bias} = 10$ V, supplying the detection circuit, the non-linearity is estimated to be 0.1% of the measured signal. For the same reason, MIO's back end lacks the grid attenuator.

After the absolute calibration procedure in 2015 a change in the bias battery type was necessary, because batteries used previously are no longer manufactured. Instead of the re-chargeable batteries, which hold the bias voltage level constant for approximately three months, batteries with the life-time of three years are used now. This exchange shifted V_{Bias} from 10 V to 7.2 V, affecting the bias current for each detection channel accordingly. As a consequence, the detector sensitivity and the noise level increase by about 10%, and a correction dependent on frequency to the absolute calibration needed to be determined and applied for both interferometers (see Section IV E 4).

III. CALIBRATION SETUP UPDATE

The calibration procedure relied on the intermediate-, cold- and heated-source. The emission spectrum of the latter source was unknown and, hence, needed to be characterised. This was achieved by the comparison with the spectra emitted by the intermediate- and cold-source. These two sources were made from a microwave absorber material held at different temperatures.

By local measurements with MIX and MIO the calibration of the diagnostic back end, the characterisation of the emission spectrum of the heated-source, and the correction to the in-vessel calibration factors due to the change of the bias battery type have been determined.

During the in-vessel calibration the heated- and the intermediate-source have been placed in front of the in-vessel antenna of MIX and MIO. With an antenna extension, the antenna pattern was investigated for MIX.

A. Calibration sources

1. Absorber material: intermediate- and cold-source

As in 2010 for local measurements the microwave absorber material TK (small tile[16]) was used. This material complies with the regulations for contamination hazards of the JET vessel. From the tiles the active surfaces were formed for the intermediate- and cold-source. While the former source was held at ambient temperature, the latter was immersed in liquid nitrogen (77 K).

The black body property of the tiles (sufficiently high absorption) which is essential for calibrating the instrument has been confirmed by local measurements down to 50 GHz, at least. This was achieved by the comparison of the measured spectrum with the one determined for another type of TK material (large tile[16]) which has the desired property even below 50 GHz. Within the uncertainties no significant difference was found.

TK material (small tile) was used to implement the intermediate-source at ambient temperature when placed in front of the in-vessel antenna. The active surface had an area of 25 cm × 25 cm which was slightly larger than the one used in 2010 (see Section III A in Ref.[12]).

2. Heated-source

For completeness, it must be mentioned that the calibration carried out in 2012 failed due to the decay of the emission spectrum of the heated-source during the in-vessel session. This source, which was newly built in that year, showed a drop in the radiative temperature of about 50 K. This drop was caused by oxidation of the heated plate made from copper. Thus, for the model built in 2015 the design was changed, and the plate was manufactured from stainless steel. In addition, prior to the 2015 in-vessel calibration the source was held at 873 K for about four weeks. For this period and right after the in-vessel sessions, the temporal evolution of the emission spectrum was investigated and no strong variations were found (see Section IV D 1).

B. Local measurements

The active surface of a source was placed centrally below the local downward pointing antenna aperture at the distance of about 12 cm. The interferogram data was acquired and stored continuously for 20 min per source. This corresponds to two independent measurements one for each moving direction of the scanning mirror. The sources have been probed sequentially, and the switching between the sources was achieved manually. The change in the ambient temperature of the intermediate-source was tracked and taken into account in the related analysis steps. Normally, a session covered the integration duration of 80 min per source corresponding to eight independent data sets. From these sets the mean and uncertainty for the quantity of interest were deduced.

Throughout two periods in 2012/13 and 2014/15, lasting each about six months, the back end calibration for MIX was tracked (see Section IV C 2). Each period comprised eleven sessions, and each session achieved a total integration duration of 160 min.

With the X-mode channel the emission spectrum of the heated-source was tracked prior to and after the in-vessel
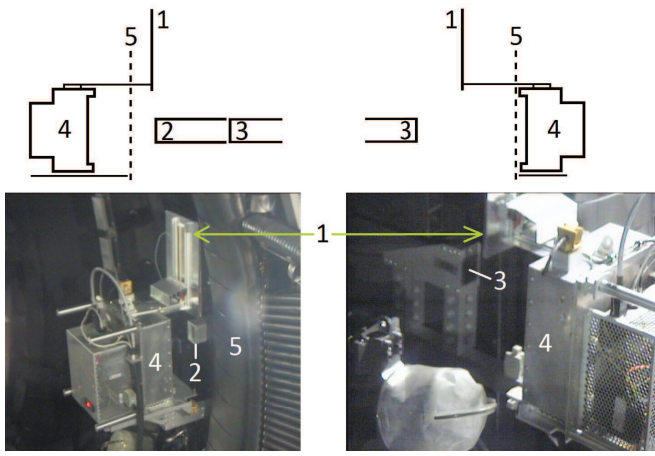
FIG. 3. Intermediate- and heated-source placed in octant 7 of JET during absolute calibration of interferometer diagnostics MIX (left) and MIO (right) in 2015. When the switch (component 1), which carries the intermediate-source (TK material), is in the down position, the diagnostic view of the heated-source (component 4) is obstructed. For the down position the active surfaces of the sources are separated by 19 cm. (Left) Investigation of antenna pattern for MIX (see session 2 in Table II). Since the limiter (component 5) prevents from positioning the heated-source closer to the antenna, an extension (component 2) is used. The distance D from the active surface of the heated-source to the aperture of the extension is about 22 cm. (Right) Calibration setup for MIO (see session 3 in Table II). No antenna extension is fitted, and the sources are placed in front of the antenna aperture (component 3), so that $D \approx 33$ cm.

calibration task for MIX (see Section IV D 1). Each of the corresponding five sessions integrated for 240 min.

The emission spectrum of the heated-source, independently probed with MIX and MIO, showed an oscillating feature below 120 GHz (see Section IV D). This feature was investigated by an extensive study, but no significant changes were found. For example the distance between the sources and the local antenna aperture was scanned, laboratory light sources were switched off, and additional shielding with matrices made from the microwave absorber material ECCOSORB was deployed.

Due to the change from re-chargeable batteries with the bias voltage of $V_{Bias} = 10$ V to long-life batteries with $V_{Bias} = 7.2$ V, the back end sensitivity changed (see Section IV E 4). This swap was done after the absolute calibration in 2015, and, hence, the calibration factors for MIX and MIO required a correction. In order to get this correction, which depends on frequency, the back end sensitivities for both sets of batteries have been probed.

C. In-vessel calibration

The stand-alone setup for the in-vessel calibration in 2015 inherited the basic features from the one used in

2010^{12}. The hot/cold technique was applied using the heated- and intermediate-source. The mounting structure and calibration sources were transportable by the remote handling system MASCOT[17] for placing inside the JET vessel. Remote control existed for the heated-source and to switch between heated- and intermediate-sources. Continuous monitoring was achieved for both physical source temperatures and the switch position, data was continuously acquired for days. No abnormal state of the calibration condition was found.

The setup of 2015 had two additional features. Firstly, for the X-mode channel an antenna extension was available to investigate the antenna pattern. Secondly, an additional mounting structure allowed the calibration of the O-mode channel.

1. Switching between sources

The intermediate-source (TK) attached to the switch was connected to the top of the outer box of the heated-source via a horizontal aluminium plate with the length of 19 cm (see component 1 in Fig. 3). The up position of the switch enabled the free view on the heated-source.

Switching between sources was carried out typically every 20 min.

2. Mounting structure

For the O-mode channel the mounting structure kept the distance D from the active surface of the heated-source to the antenna aperture fixed at about 33 cm. For the X-mode channel, the mounting structure offered the possibility to change the distance from about 33 cm to 63 cm (see Fig. 3 left). This allowed the investigation of the antenna pattern in combination with the antenna extension.

3. Overall control and monitoring program

New calibration software with the same functionality as in 2010, for example controlling the source device including the switch, monitoring parameters and acquiring data, was implemented in the programming language Python and was available as a web service inside the JET network.

4. Antenna extension

The extension with the length of 23 cm was designed to allow the fitting onto the in-vessel antenna for the X-mode channel remotely via MASCOT. The antenna aperture (inner dimensions 50 mm $\times$ 65 mm $\times$ 3 mm wall thickness) was enclosed tightly by the extension with the inner dimensions 57 mm $\times$ 71 mm. With the extension in

Session	1	2	3
Diagnostic	MIX	MIX	MIO
Distance D (cm)	33	22	33
Extension in place	no	yes	no
Integration time (h)	90	45	60
$N_{\Delta V}$	272	134	184
Mean of T_{IS} (K)	318.01	316.88	316.25
Uncertainty of T_{IS} (K)	±1.16	±0.62	±0.41

TABLE II. Main parameters for in-vessel calibration sessions in 2015 like distance D between active surface of heated-source and antenna/extension aperture, number $N_{\Delta V}$ of valid difference interferograms (each reflects 20 min integration duration) available, session mean and uncertainty of physical temperature T_{IS} of intermediate-source.

place (see component 2 in Fig. 3 left) the aperture shifted towards the calibration sources, and, hence, the source device needed to be moved on the mounting structure, so that the switch was able to operate.

5. In-vessel task: three calibration sessions

In 2015 three in-vessel sessions, two for MIX and one for MIO, have been carried out (see Table II). The first session for MIX was used to replicate the 2010 calibration conditions, keeping the active surface of the heated-source from the antenna aperture at the distance $D \approx$ 33 cm. One day after the first session (total integration time of about 90 hours) had ended, the second session started to investigate whether the antenna pattern was filled with the heated-source at $D \approx 33$ cm. This session made use of the antenna extension, and the sources
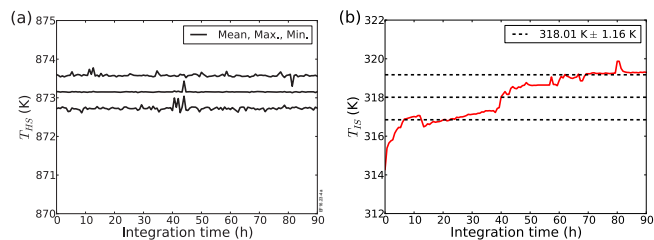

FIG. 4. Physical temperatures T_{HS} and T_{IS} of heated- and intermediate-source dependent on integration time for first MIX in-vessel session. Although being probed every second, the presented quantities characterise the state of the sources on the temporal grid of 40 min. (a) Mean, maximum and minimum of T_{HS}. The temperature of the heated-source is held in the window 873 K ± 0.5 K by the control software. (b) Mean of T_{IS} (solid). T_{IS} is continuously rising due to heat radiated by the heated-source. For the whole session T_{IS} is summarised by 318.01 K and the uncertainty of ±1.16 K (dashed).

were moved, so that $D \approx 22$ cm (see Fig. 3 left). The integration time was 45 hours.

The third session was dedicated to calibrate MIO. No extension was in place, and the heated-source has been kept at a location for which $D \approx 33$ cm (see Fig. 3 right).

During the three sessions the physical temperature T_{HS} of the heated-source showed little variation of ±0.5 K in the vicinity of 873 K, for example see Fig. 4(a) for the first MIX session.

Influenced by the heated-source, the temperature T_{IS} of the intermediate-source was changing throughout the integration period (see Fig. 4(b)). However, its variation was of the order of ±1 K and was taken into account in the estimation of the calibration uncertainties.

IV. ANALYSIS

A. Diagnostic model

1. Ideal instrument

The ideal Martin-Puplett interferometer probes two spectra I_1 and I_2 carried in perpendicular polarisation directions and coupled into the diagnostic by the two input ports. The following beam splitter mixes the polarisations equally and generates two partial beams by transmission and reflection towards two separate arms. Usually, as it is the case at JET, the rooftop mirror located in one arm is spatially fixed, while the other moves. The reflection at each mirror flips the polarisation by 90 degrees, so that the returning beams are reflected and transmitted by the beam splitter, respectively. This allows the recombination of the partial beams which have now an optical path difference x with respect to each other due to the mirror movement causing an interference pattern.

Starting from the transposed input quantity $\vec{I}_{in}^T = (I_1, I_2)$ the interferometer generates

$$\vec{I}_{out} = \frac{I_1 + I_2}{2} \begin{pmatrix} 1 + \frac{I_1 - I_2}{I_1 + I_2} \cos\left(2\pi \frac{f}{c} x\right) \\ 1 - \frac{I_1 - I_2}{I_1 + I_2} \cos\left(2\pi \frac{f}{c} x\right) \end{pmatrix}. \quad (1)$$

In the above equation the frequency f is used instead of the natural counterpart for the spatial coordinate x, i.e., the wavenumber $\nu = f/c$ involving the speed of light. Three facts are worth mentioning. Firstly, the total intensity is preserved. Secondly, the sum spectrum appears in both components of $\vec{I}_{out}$. Finally, the difference spectrum $\Delta I = I_1 - I_2$ is cosine transformed and carries opposite signs in the two components of $\vec{I}_{out}$ marking constructive and destructive interference. This implies that an additional polariser is mandatory to separate the two interfering components. Then, at the output ports the cosine transform of ΔI, i.e., the interferogram

$$V_{\pm}(x) = \pm \frac{1}{2} \int_0^\infty \Delta I \cos\left(2\pi \frac{f}{c} x\right) df + V_{DC} \quad (2)$$

is observable varying around the absolute term $V_{DC} = \int (I_1 + I_2) df / 2$.

2. Real world instrument

In practice, several features need to be taken into account to model a real world diagnostic. The two intensity spectra I_1 and I_2 are available at the associated antenna and guided by the transmission line to the input port. For the first diagnostic arm the spectral flux P_1 coupled by the antenna into the transmission line can be written as

$$P_1 = 4\pi \langle I_1 \rangle \langle G_1 \rangle A_1, \tag{3}$$

using the mean spectrum

$$\langle I_1 \rangle = \frac{\int\limits_{A_1} \int\limits_{4\pi} I_1(\vec{r}, \Omega) G_1(\vec{r}, \Omega) d\Omega d\vec{r}}{\int\limits_{A_1} \int\limits_{4\pi} G_1 d\Omega d\vec{r}} \tag{4}$$

and the mean antenna gain

$$\langle G_1 \rangle = \frac{\int\limits_{A_1} \int\limits_{4\pi} G_1 d\Omega d\vec{r}}{\int\limits_{A_1} \int\limits_{4\pi} d\Omega d\vec{r}}, \tag{5}$$

and the integrals are performed with respect to the solid angle Ω and the surface area A_1 of the antenna aperture. The transmission line transfers P_1 to the input port of the interferometer, while attenuating P_1 by the factor D_{T1} and emitting itself P_{T1}. Accordingly, at the first input port of the diagnostic $4\pi \langle I_1 \rangle \langle G_1 \rangle A_1 D_{T1} + P_{T1}$ is available, and for the second input port a similar quantity is derived. Assuming that both partial beams have the same throughput τ until the detector with the sensitivity S_D is reached, one finds for the constructive case

$$V_+(x) = \frac{1}{2} \int_0^\infty \left(\langle I_1 \rangle C_{f,1} - \langle I_2 \rangle C_{f,2} \right) \cos \left(2\pi \frac{f}{c} x \right) df +$$
$$+ \frac{1}{2} \int_0^\infty \left(P_{T1} - P_{T2} \right) \tau S_D \cos \left(2\pi \frac{f}{c} x \right) df +$$
$$+ V_{DC} \tag{6}$$

with the diagnostics sensitivities $C_{f,1(2)} = 4\pi \langle G_{1(2)} \rangle A_{1(2)} D_{T1(2)} \tau S_D$ for the two inputs and the absolute value $V_{DC} = \int (\langle I_1 \rangle S_1 + \langle I_2 \rangle S_2 + (P_{T1} + P_{T2}) \tau S_D) df / 2$. The post-detection amplification electronics removes the constant quantity V_{DC} and augments the interfering part by the factor A. This amplified signal is sampled at a finite set x_i of optical path difference locations. In addition, an asymmetric feature, caused by dispersion, misalignment and/or changing power coupling to the detection section for the partial beam which passes through the arm with variable length, is taken into account by the phase α' which is added to the cosine argument. Furthermore, since only one, say the first, diagnostic arm is of importance, one can write

$$V'(x_i) = \frac{A}{2} \int_0^\infty \langle I_1 \rangle C_{f,1} \cos \left(2\pi \frac{f}{c} x_i + \alpha' \right) df +$$
$$+ V_0(x_i) + B(\langle I_1 \rangle, x_i) + \mathcal{N}(0, \sigma) + V_M \tag{7}$$

where V_0 marks all contributions which are independent of $\langle I_1 \rangle$, i.e., the remaining terms of equation (6) and any other term being not included in this deduction. The final form of the diagnostic model stated in equation (7) includes three imperfections: the source-dependent background B, the noise contribution $\mathcal{N}$, and spurious signal appearance V_M. The source-dependent background B marks a drifting offset over large spatial scales and is caused by the power coupling for one partial beam to the detection system which depends itself on x. Hence, at a fixed location x_i B changes when $\langle I_1 \rangle$ does. A nondeterministic imperfection is the noise term $\mathcal{N}$ which is characterised by Gaussian white noise with vanishing mean and standard deviation σ in very good approximation. The term V_M abbreviates spurious signals, allegedly picked up by the diagnostic from radio and mobile phone emission. Fortunately, these signals are rarely present and, since V_M is of the order of some Volts, are identifiable and removable especially during calibration tasks.

Alternatively to this model, one can use the Rayleigh-Jeans law to express the intensity spectrum $I_1 = 2k_B f^2 T_1^{Rad} / c^2$ by the radiative temperature T_1^{Rad} via the Boltzmann constant k_B. This modifies the kernel of the spectral integral in equation (7) to

$$\langle I_1 \rangle C_{f,1} = \langle T_1^{Rad} \rangle \left(2k_B f^2 C_{f,1} / c^2 \right) = \langle T_1^{Rad} \rangle C_{T,1} \tag{8}$$

It can be seen from the diagnostic model, that if the imperfections are dealt with and the optical path difference grid and the phase is at hand, either the instrument can be calibrated absolutely or a spectrum can be characterised in absolute terms. For these two modi operandi the first analysis steps are similar, and, therefore, will be presented together in the following paragraph.

B. From Spatial Quantities to Spectral Quantities

1. Difference Interferogram/Interferogram

For calibration tasks the noise $\mathcal{N}(0, \sigma)$ is reduced sufficiently by averaging about 35×10^3 individual interferograms coherently for probing the same calibration source. Thereby, spurious signals V_M are identified and digitally filtered (as described in Section IV B in[12]). Using the difference interferogram $\Delta V'$, which is given by the difference of two averaged interferograms acquired for different sources, removes V_0 in equation (7). As a consequence the model becomes

$$\Delta V'(x_i) = \frac{A_C}{2} \int_0^\infty \Delta S' \cos \left(2\pi \frac{f}{c} x_i + \alpha' \right) df + \tag{9}$$
$$+ B(\langle I_1 \rangle - \langle I_2 \rangle, x_i) + \mathcal{N}(0, \sigma \times \sqrt{2/35000})$$

where the difference spectrum $\Delta S' = (\langle I_1\rangle - \langle I_2\rangle)\,C_{f,1}$ has been introduced for later purposes, and the gain A_C for calibration was set.

For plasma operation the SNR is sufficiently large, and, thus, the data analysis deals with individual interferograms V'. Moreover, V_0 is negligible, and the spurious signal contribution V_M is left out, since it is rarely observed during a JET pulse of about 30 s. Then the plasma model is stated by

$$V'(x_i) = \frac{A_P}{2}\int_0^\infty S'\cos\left(2\pi\frac{f}{c}x_i + \alpha'\right)df +$$
$$+ B(\langle I_1\rangle, x_i) + \mathcal{N}(0, \sigma \times A_P/A_C) \qquad (10)$$

with the spectrum $S' = \langle I_1\rangle C_{f,1}$ and the amplification A_P.

In general, the data vectors $\Delta V'$ and V' depend on the data index i and contain at least 800 values.

2. Estimation and removal of source-dependent background

Even for a well aligned interferometer back end the power coupling of one partial beam to the receiving circular antenna (see component 9 in Fig 3 in Ref.[12]), located just in front of the detector, depends on the optical path difference x between the two beams. This variable coupling is caused by the change in the solid angle of the circular antenna aperture with respect to the moving mirror, while the corresponding solid angle with respect to the fixed mirror remains constant. The ratio $L^2/(L+x)^2$ of both solid angles, where L is the optical path length for the partial beam passing through the fixed arm, measures the relative power coupling. Because L is of the order of 600 mm, and x varies between -6 mm and 28 mm, which is small compared to L, it can be expected that the background B is well approximated by a ramp with a small quadratic feature. Hence, the background is modelled by a second order polynomial $B(i) = a_0 + a_1 i + a_2 i^2$ where i is the data index connected to the optical path difference x_i (see Section IV B 3).

B parameterised in the three coefficients can be estimated with a polynomial regression fit for which the partial derivatives in a_0, a_1 and a_2 of $\sum_i \left(\Delta V'_i - (a_0 + a_1 i + a_2 i^2)\right)^2$ vanish. The background is removed giving $\Delta V = \Delta V' - B$ and $V = V' - B$, respectively.

For local measurements, in general, the obtained difference interferograms $\Delta V_{HS,IS}$ (heated/intermediate-source combination) and $\Delta V_{IS,CS}$ (intermediate/cold-source combination) vary nicely around zero (see example for MIX in Fig. 5(a)). Furthermore, as expected the linear term of the background is of leading order as the collection $(4\times B_{HS,IS}$ and $4\times B_{IS,CS})$ presented in Fig. 5(b) demonstrates. In addition, the backgrounds estimated are very similar for the same source combination, and $B_{HS,IS}$ is about twice in amplitude as $B_{IS,CS}$. The

latter fact can be explained by the ratio $2.1 \approx$ (750 K - 293 K)/(293 K - 77 K) of the difference intensities for the source which is evaluated from the involved radiative temperatures (see Section IV D for heated-source).

For plasma operation the situation becomes more complicated, since a source-related effect is present on top of the diagnostic effect described above. Due to fast events, like sawtooth activity inside the plasma, the ECE spectrum can vary on faster time scales than the diag-
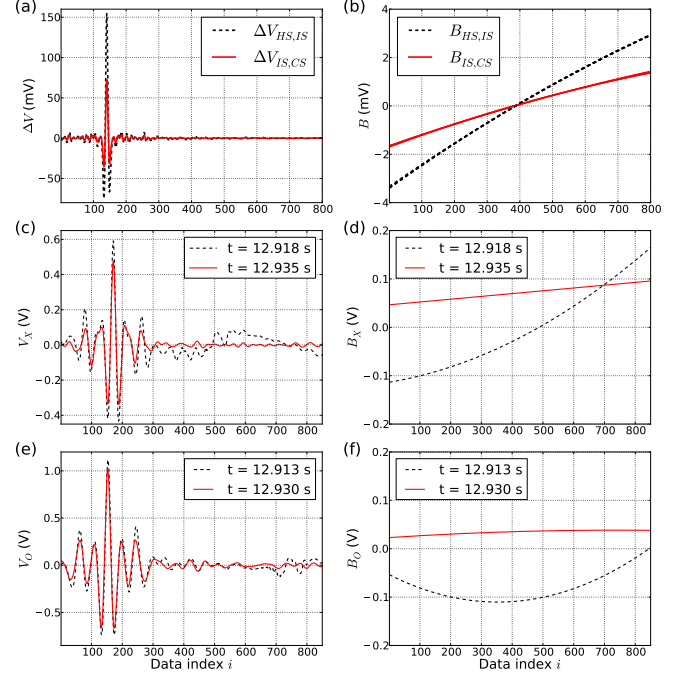

FIG. 5. Source-dependent background B estimated (right column) and remaining difference interferograms ΔV and interferograms V (left column) dependent on data index i. B modelled by a polynomial of second order is estimated via a regression fit. (a) Two difference interferograms $\Delta V_{HS,IS}$ (dashed) and $\Delta V_{IS,CS}$ (solid) obtained with interferometer MIX during local measurements. From three interferograms for the heated-source (HS), the intermediate-source (IS) and the cold-source (CS) the two difference interferograms $\Delta V_{HS,IS} = V_{HS} - V_{IS} - B_{HS,IS}$ and $\Delta V_{IS,CS} = V_{IS} - V_{CS} - B_{IS,CS}$ follow. $\Delta V_{HS,IS}$ and $\Delta V_{IS,CS}$ vary around the zero-baseline. (b) Backgrounds $B_{HS,IS}$ (4×dashed) and $B_{IS,CS}$ (4×solid). Clearly, the background depends on the source combination and is very similar in shape for independent measurements for a fixed source combination. The linear term is dominating. (c) and (e) Two interferograms V_X and V_O measured with MIX and MIO during JET pulse 89074. While V_O and V_X (both dashed) at times t = 12.913 s and t = 12.918 s are affected by fast temporal changes in the ECE spectrum, caused for example by sawtooth activity inside the plasma, the subsequent interferograms (both solid) behave regularly again. (d) and (f) B_X and B_O associated with interferograms presented in (c) and (e). Temporal changes in the ECE spectra faster than the diagnostic temporal resolution of 17 ms are identifiable by the linear and/or the quadratic term, since their amplitudes are increased by at least one order of magnitude.

nostic temporal resolution of 17 ms. As a consequence, distorted interferograms V_X and V_O are evident for the X- and O-mode channel (see black curves in Fig. 5(c) and (e)). The affected interferograms can be identified by the estimated linear and the quadratic coefficients of the background which have large amplitudes (see black curves in Fig. 5(d) and (f)). Usually, regular interferograms (see red curves in Fig. 5(c) and (e)) follow subsequent to an unsuitable one.

When B is removed,

$$\Delta V = \frac{A_C}{2} \int_0^\infty \Delta S' \cos \left(2\pi \frac{f}{c} x_i + \alpha' \right) df \quad (11)$$

remains, ignoring the noise contribution. The above equation can be treated with standard methods described below.

3. Optical path difference grid

So far no optical path difference value x_i is assigned to the i-th entry of the data vector ΔV or V. Since the spatial sampling of the interferogram is triggered when the optical path difference has changed by the increment $\Delta x = 40$ μm, the ansatz $x_i = i\Delta x + x_{ZPD}$ for the optical difference grid is justified. Thereby, the zero-path difference x_{ZPD} is the only unknown quantity. Generally, x_{ZPD} marks the position of the global extremum (here maximum), and, hence, for an interferogram, being hypothetically continuous, $d(\Delta V)/dx$ must vanish. For a discrete data set the simplest way to estimate x_{ZPD} is the fit of a parabola to the three values ΔV_{m-1}, ΔV_m and ΔV_{m+1} which are closest to the data index m of the maximum of the set ΔV. In doing so, the relative shift

$$\eta = 0.5 \frac{\Delta V_{m+1} - \Delta V_{m-1}}{2\Delta V_m - \Delta V_{m+1} - \Delta V_{m-1}}. \quad (12)$$

is found which results in $x_{ZPD} = -(m+\eta)\Delta x$. With this definition reasonable values for η are located in the interval [-0.5, 0.5].

According to the Nyquist theorem spectral quantities can be probed up to maximum frequency $f_{Max} = c/(2\Delta x) = 3747$ GHz.

With the optical path difference grid available a common spatial domain is identified which is used in further analysis steps for plasma operation and calibration. This domain comprises the double-sided region $|x| < 5.12$ mm ($= L_{DS}$) and the single-sided region 5.12 mm $< x \leq$ 26.4 mm ($= L_{DS} + L_{SS}$). This choice ensures that the double-sided domain contains always $N_{DS} = 256$ ($=2^8$) measured values, and the single-sided region holds $N_{SS} = 532$ data points. This limitation of the spatial domain causes an adaption of the zero-path difference by

$$x_{ZPD} = -(N_{DS}/2 + \eta)\Delta x + \begin{cases} 0 & : \eta \leq 0 \\ \Delta x & : \eta > 0 \end{cases} . \quad (13)$$

4. Window functions

In general, Fourier spectroscopy diagnostics probe a finite optical path difference domain. Hence, the acquired interferogram data starts and ends abruptly. Since the classical approach does not deal with the non-probed spatial domain, apodisation functions, also called window functions, are used to bring an interferogram smoothly to zero towards the spatial edges.

Basically, a window function dependent on x is multiplied with the interferogram to achieve a certain convolution function in the spectral domain. Two apodisation functions W_α and W_S are mandatory to derive the phase α and the difference spectrum ΔS or spectrum S, respectively.

W_α is symmetric with respect to the spatial origin and is finite only for the double-sided interferogram region. Due to this symmetry the original even and odd parts of the interferogram are preserved, if the deduced spatial origin equals the true value.

Usually, W_S assigns a higher weighting to the single-sided spatial domain with respect to the one for the double-sided region. This decreases the width of the convolution function, and, therefore, increases the spectral resolution.

At JET, W_α has a triangular shape with the centre at the zero-path difference (see Fig. 6(a)). The main window function W_S is defined for the domain -5.12 mm to 35.84 mm ($= L_{DS} + L_{SS} + L_{ZP}$) where $L_{ZP} = 9.44$ mm is the length of the domain which is zero-padded. W_S consists of a ramp in the double-sided domain and a quarter-period cosine function in the single-sided domain and is zero outside of those two domains (see Fig. 6(a)). Formally, one gets

$$W_\alpha = 1 - \frac{|x|}{L_{DS}} \quad : |x| \leq L_{DS} \quad (14)$$

and

$$W_S = \begin{cases} \frac{x + L_{DS}}{2L_{DS}} & : |x| \leq L_{DS} \\ \cos\left(\pi \frac{x - L_{DS}}{2L_{SS}}\right) & : L_{DS} < x \leq L_{DS} + L_{SS} \\ 0 & : L_{DS} + L_{SS} < x \leq L_{ZP}. \end{cases} \quad (15)$$

Both window functions are evaluated at $N_{DS} = 256$ and $N_T = 1024$ points, where N_{DS} and N_T are powers of two to comply with the condition for the discrete fast Fourier transformation.

5. Convolutions for window functions

In the field of Fourier spectroscopy convolution is inevitable. The convolution function for a given window function W is evaluated by

$$Conv = \sum_i W(x_i) \left[\cos\left(2\pi \frac{f'}{c} x_i \right) + \sin\left(2\pi \frac{f'}{c} x_i \right) \right] \times$$
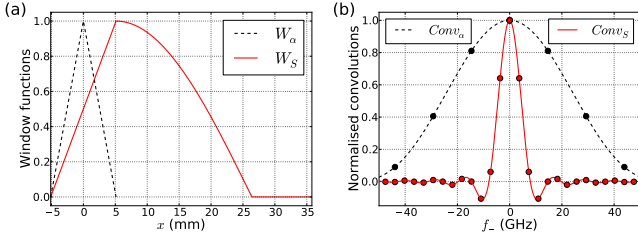
FIG. 6. Window functions W_α and W_S in spatial domain and associated normalised convolution functions $Conv_\alpha$ and $Conv_S$ captured here by $DFT_{\cos}\{W_\alpha\}$ and $DFT_{\cos}\{W_S\}$ in spectral domain. (a) W_α (dashed), W_S (solid) dependent on optical path difference x. W_α has a triangular shape centred at the origin and is finite in the double-sided domain $|x| \leq L_{DS} = 5.12$ mm. For this domain W_S is given by a ramp. In the single-sided region W_S equals the first quarter period of a cosine vanishing at 26.4 mm. In the domain 26.4–35.8 mm W_S is zero-padded. (b) $DFT_{\cos}\{W_\alpha\}$ (dashed) and $DFT_{\cos}\{W_S\}$ (solid) dependent on difference frequency f_-. The spectral resolutions $\delta_f \approx \pm20.8$ and ±2.8 GHz are achieved with $Conv_\alpha$ and $Conv_S$. The phase and the (difference) spectrum $(\Delta)S$ are evaluated at the frequency grid (dots) with increment $\Delta_f \approx 14.64$ and 3.66 GHz, respectively. Due to zero-padding ($\delta_f/\Delta_f > 1/2$) values of $(\Delta)S$ obtained at neighbouring frequencies have an elevated correlation.

$$\times \left[\cos\left(2\pi\frac{f}{c}x_i\right) + \sin\left(2\pi\frac{f}{c}x_i\right)\right]\Delta x. \quad (16)$$

Using trigonometric identities one finds the sum and difference frequencies $f_+ = f' + f$ and $f_- = f' - f$ on the right-hand side. The convolution applied to a function, say a spectrum $S'(f')$, is expressed by $S(f) = \int S(f')Conv(f', f)df'$. Since only a finite spatial domain is probed, $Conv(f', f)$ has a finite width, and, hence, the spectral resolution is finite.

The window functions W_α and W_S applied in the spatial domain correspond to the convolution functions $Conv_\alpha$ and $Conv_S$ in the spectral domain. To characterise the widths of the convolution functions, and, hence, the spectral resolution the discrete cosine Fourier transforms $DFT_{\cos}\{W_\alpha\}(f_-)$ and $DFT_{\cos}\{W_S\}(f_-)$ are evaluated numerically on a fine spectral grid (see Fig. 6(b)). The results are symmetric with respect to $f_- = 0$, where, in addition, the global maximum is located. For $DFT_{\cos}\{W_S\}$ the maximum has the value $(2N_{SS}/\pi + (N_{DS}+1)/2)\Delta x$ which is important to connect a defined calibration factor with the actual diagnostic sensitivity. $DFT_{\cos}\{W_\alpha\}$ has a larger full width at half maximum (FWHM) of about 52 GHz compared with the FWHM of 9 GHz for $DFT_{\cos}\{W_S\}$. Away from $f_- = 0$ both functions approach zero asymptotically.

The spectral resolution δ_f, associated with a convolu-

tion function, is captured here by the condition

$$\frac{\int_0^{\delta_f} DFT_{\cos}\{W\}df_-}{\int_0^\infty DFT_{\cos}\{W\}df_-} = 0.66. \quad (17)$$

With this convention one finds numerically the resolutions $\delta_f \approx \pm20.8$ GHz and ±2.8 GHz for $Conv_\alpha$ and $Conv_S$, respectively.

6. Phase and (difference) spectrum

To retrieve the phase α the discrete sine and cosine fast Fourier transforms $DFFT_{\sin}$ and $DFFT_{\cos}$ of the product $W_\alpha\Delta V$ or $W_\alpha V$ are evaluated. To keep the functionality general in diverse programming languages, the implementations of the two transforms do not take into account any information about the zero-path difference x_{ZPD}. Hence, the subtraction of an additional ramp is necessary to extract the phase via

$$\alpha''(f_j) = modulo\left[-2\pi\frac{j\Delta'_f}{c}x_{ZPD} - \quad (18)\right.$$

$$\left. -\arctan\left(\frac{DFFT_{\sin}\{W_\alpha\Delta V\}(j)}{DFFT_{\cos}\{W_\alpha\Delta V\}(j)}\right) + \pi, 2\pi\right] - \pi$$

and x_{ZPD} is taken from expression (13). The phase is evaluated on the spectral grid $f_j = j\Delta'_f$ with the increment $\Delta'_f = c/(2N_{DS}\Delta x) \approx 14.64$ GHz. Finally, since the difference spectrum (or spectrum) is evaluated on the finer spectral grid $f_k = k\Delta_f$ with the increment $\Delta_f = \Delta'_f N_{DS}/N_T \approx 3.66$ GHz up to the Nyquist frequency $f_{Max} = 3747$ GHz, a linear interpolation projects $\alpha''(f_j)$ to $\alpha(f_k)$.

Ideally, the difference spectrum ΔS would be evaluated by

$$\Delta S(f_k) = \Delta x \times$$

$$\times \left[DFFT_{\cos}\{W_S\Delta V\}(k)\cos\left(2\pi\frac{f_k}{c}x_{ZPD} + \alpha\right) - \right.$$

$$\left. -DFFT_{\sin}\{W_S\Delta V\}(k)\sin\left(2\pi\frac{f_k}{c}x_{ZPD} + \alpha\right)\right] \quad (19)$$

given x_{ZPD} and phase α and having the background removed. Similarly, the spectrum S is obtained by replacing ΔV with V.

Note, α and ΔS (or S) are average values of α', $\Delta S'$ (or S') in the diagnostic model (see equations (9) and (10)) weighted by $Conv_\alpha$ and $Conv_S$ (see Section IV B 5 and Fig. 6(b)) mainly in the spectral domain $f_k\pm 20.8$ GHz and $f_k\pm 2.8$ GHz, respectively. Furthermore, neighbouring frequencies probe ΔS in partly overlapping domains ($\delta_f/\Delta_f = 2.8$ GHz/3.66 GHz $> 1/2$) caused by the zero-padding of the main window function W_S.

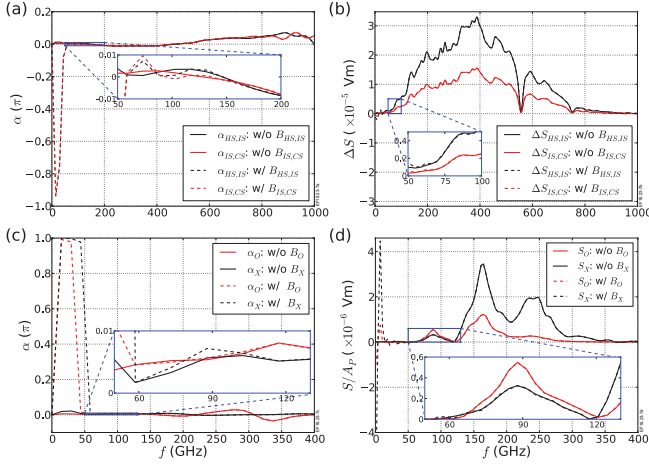Figure 7 presents some examples for the phase, difference spectrum and spectrum, evaluated with and without

FIG. 7. Phase α, difference spectrum ΔS and spectrum S dependent on frequency f. The spectral quantities are evaluated having the background B from the data removed (solid) and not removed (dashed). While the first row shows results for local measurements with the interferometer MIX (see Fig. 5 (a) and (b)), the second row presents the outcome for probing a JET plasma (pulse 89074) with MIO at time t = 12.879 s and with MIX at t = 12.883 s. Without B the results are smoother and remain small towards the origin, and ΔS and S with and without B can deviate by some percentage in the range 50–120 GHz. (a) $\alpha_{HS,IS}$ (black) and $\alpha_{IS,CS}$ (red). (b) $\Delta S_{HS,IS}$ (black) and $\Delta S_{IS,CS}$ (red). (c) α_X (black) and α_O (red). (d) S_X (black) and S_O (red) scaled with amplification A_P for plasma operation. For MIX and MIO A_P is set to $10^{2.2}$ and 10^3, respectively.

the associated background B. Without B, α is small, and ΔS and S approach zero smoothly for frequencies below 50 GHz and above some hundreds GHz for both interferometers. In general, these spectral quantities are smoother below 150 GHz as the one for having B included in the data, and, in addition, deviations of a few percentage are evident for the range 50–120 GHz. Towards the origin, the removal of B affects heavily the determination of the spectral quantities.

C. Absolute calibration: diagnostic back end

1. Observable and JET Definitions

On the temperature scale the observable diagnostic sensitivity is obtained by

$$\hat{C}_{T,1}(f_k) = \frac{\Delta S_{1S,2S}(f_k)}{\frac{A_C}{2}\frac{1}{2}\int\limits_{-\infty}^{\infty}\langle\Delta T_{1S,2S}^{Rad}\rangle Conv_S(f,f_k)df}, \quad (20)$$

assuming the radiative temperatures $\langle\Delta T_{1S}^{Rad}\rangle$ and $\langle\Delta T_{2S}^{Rad}\rangle$, and, hence, their difference $\langle\Delta T_{1S,2S}^{Rad}\rangle$ at the antenna aperture are known. If $\langle\Delta T_{1S,2S}^{Rad}\rangle$ is constant in

frequency, then one finds the approximation

$$\int\limits_{-\infty}^{\infty} Conv_S(f,f_k)df = 2\int\limits_{0}^{\infty} DFT_{\cos}\{W_S\}df_- \approx$$

$$\approx \frac{4N_{SS}/\pi + N_{DS} + 1}{2N_{SS} + N_{DS} + 1}c \quad (21)$$

for the JET case, exploiting the relation $\Delta x\delta_f = c/(2N_{SS} + N_{DS} + 1)$.

Besides the theoretical observable quantity, at JET the calibration on the temperature scale is defined as

$$C_T(f_k) = \frac{1}{2A_C}\frac{\Delta S_{1S,2S}}{\Delta T_{1S,2S}^{Rad}} \quad (22)$$

using the physical temperatures T_{1S}^{Rad} and T_{2S}^{Rad}, and their difference $\Delta T_{1S,2S}^{Rad}$, of two calibration sources. The ratio approximated by

$$\frac{\hat{C}_{T,1}}{C_T} = 8\frac{\Delta T_{1S,2S}^{Rad}}{\langle\Delta T_{1S,2S}^{Rad}\rangle}\frac{2N_{SS} + N_{DS} + 1}{4N_{SS}/\pi + N_{DS} + 1}\frac{1}{c} \quad (23)$$

reveals the conversion factor between the calibration and the observable diagnostic sensitivity. Furthermore, if the antenna pattern is filled for each calibration source, the ratio $\Delta T_{1S,2S}^{Rad}/\langle\Delta T_{1S,2S}^{Rad}\rangle$ becomes unity.

A similar derivation can be done using the intensity scale for which at JET the definition

$$C_f = \frac{1}{2A_C}\frac{\Delta S_{1S,2S}}{\Delta I_{1S,2S}} \quad (24)$$

is used.

2. MIX: long-term study

The back end calibration $C_{T,X}^{BE}$ of MIX was investigated in a long-term study carried out during two periods in 2012/13 and 2014/15. That is in total 22 sessions giving each eight independent data sets. The corresponding session means for $C_{T,X}^{BE}$ show a wider spread for higher frequencies (see Fig. 8(a)). Excluding domains with strong atmospheric absorption, each mean is determined with the relative uncertainty, defined as standard deviation of the session mean divided by the session mean, of less than $\pm15\%$ for the range from 30 to 900 GHz and less than $\pm0.4\%$ for the range from 150 to 500 GHz (see Fig. 8(c)). Furthermore, the relative uncertainty for different sessions are very similar, and, hence, the precision of the measurement seems to remain preserved throughout months and years. However, this precision is poor for spectral domains affected by absorption by water vapour (for example at 557 GHz) and oxygen (around 55 GHz).

The period means $C_{T,X}^{BE,2013}$ and $C_{T,X}^{BE,2015}$, each evaluated as the mean of the eleven session means, are very close to each other (see Fig. 8(b)). Furthermore, the mean ratio $C_{T,X}^{BE,2013}/C_{T,X}^{BE,2015}$ varies around unity at
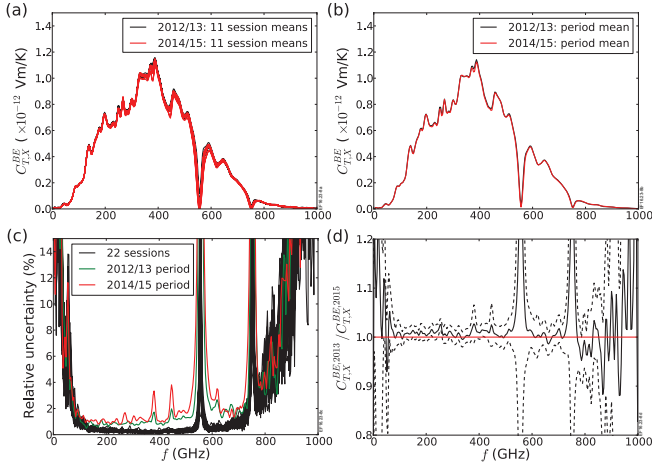
FIG. 8. Long-term study of back end sensitivity $C_{T,X}^{BE}$ dependent on frequency f for interferometer MIX carried out during two periods in 2012/13 and 2014/15. (a) Session means for periods in 2012/13 (black) and in 2014/15 (red). The sensitivity changes more in magnitude for higher frequencies on the time scale of weeks and months. (b) Period means for sessions in 2012/13 (black) and in 2014/15 period (red). $C_{T,X}^{BE}$ changes less over years (see also (d)) than over weeks and months (see (a)). (c) Relative uncertainties of $C_{T,X}^{BE}$ for individual sessions (black) and both periods (green and red). While during a session $C_{T,X}^{BE}$ is determined with highest precision ($\ll 1\%$) for the spectral domain from 100 to 500 GHz, the relative uncertainty increases to a value between 1% and 2% in the long-term. Furthermore, the study reveals the enhanced influence of atmospheric absorption at 380, 448, 557, 621 and 752 GHz. (d) Ratio of period means (solid) with uncertainties (dashed) determined with Gaussian error propagation. Within the uncertainties the ratio remains close to unity for the spectral domain from 60 to 700 GHz except regions affected by atmospheric absorption.

least within the uncertainty determined with Gaussian error propagation (see Fig. 8(d)). Thus, the back end sensitivity changes little over years. However, temporal variations on shorter time scales are evident by comparing the 22 session means with the two period means. These variations are estimated by the relative uncertainty which is given by dividing the standard deviation of the period mean by the period mean $C_{T,X}^{BE,2013}$ and $C_{T,X}^{BE,2015}$, respectively (see green and red curve in Fig. 8(c)). During long time periods the absolute sensitivity varies relatively by about $\pm 1.5\%$ in the range 100–500 GHz. In addition, an increase of the relative uncertainty becomes visible and quantifiable around water vapour absorption lines at 380, 448, 557, 621 and 752 GHz.

3. MIO

Due to set-up tasks like optical alignment the sensitivity $C_{T,O}^{BE}$ of MIO's back end could not be studied for extended periods. The sensitivity $C_{T,O}^{BE}$, determined by
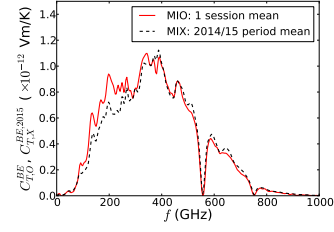
FIG. 9. Back end calibration $C_{T,O}^{BE}$ (solid) of interferometer MIO and $C_{T,X}^{BE,2015}$ (dashed) of interferometer MIX. While $C_{T,O}^{BE}$ is determined from a single session, $C_{T,X}^{BE,2015}$ was evaluated from eleven sessions (see Section IV C 2). Both diagnostics have similar sensitivities up to 1000 GHz. Since dips in $C_{T,O}^{BE}$ occur where water vapour absorption lines are supposed to be, for example at 557 and 752 GHz, the assumed spatial sampling with the increment $\Delta x = 40$ μm is achieved well enough, so that the spectral grid can be trusted.

one calibration session, is similar to the one of MIX and even exceeding it below 350 GHz (see Fig. 9). The relative uncertainty for this measurement behaves like the X-mode channel one (see black curves in Fig. 8(c)).

The dips in the sensitivity for MIO coincide with the locations of the water vapour absorption lines, for example at 557 and 752 GHz. Hence, the achieved spatial sampling of the interferogram must be close to the assumed one, having the constant increment $\Delta x = 40$ μm (see Section IV B 3).

D. Radiative temperature of heated-source

After obtaining the back end calibration $C_T^{BE}(f_k)$, the emission spectrum of the heated-source (HS), which is held at the physical temperature of 873 K (600 C), is determined. From the corresponding difference spectrum $\Delta S_{HS,IS}(f_k)$ (see Fig. 7(b)) the emission spectrum expressed in terms of radiative temperature follows from

$$T_{HS}^{Rad}(f_k) = \frac{1}{2A_C}\frac{\Delta S_{HS,IS}}{C_T^{BE}} + T_{Amb}. \qquad (25)$$

The ambient temperature T_{Amb} is measured in situ.

1. Long-term study using MIX

Using MIX the temporal evolution of the radiative temperature $T_{HS,X}^{Rad}$ was investigated by 5 sessions, starting from four weeks prior to the in-vessel task to five days after. Throughout the first weeks the emission decreases slightly, for example about 10 K around 500 GHz and about 5 K for the range from 100 to 200 GHz. However, for the fourth and fifth session, allocated just before and after the in-vessel task, the means of $T_{HS,X}^{Rad}$ are alike within the uncertainties. Therefore, it is assumed that the variation of $T_{HS,X}^{Rad}$ is negligible during the in-vessel
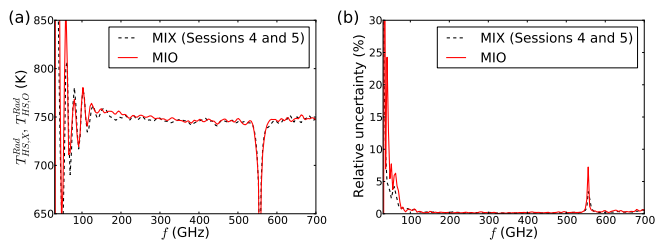
FIG. 10. Radiative temperatures $T_{HS,X}^{Rad}$ and $T_{HS,O}^{Rad}$ of heated-source held at physical temperature 873 K for spectral domain 30–700 GHz. The corresponding data sets have been acquired independently with MIX and MIO. (a) $T_{HS,X}^{Rad}$ (dashed) and $T_{HS,O}^{Rad}$ (solid) used to derive calibration factors for MIX and MIO. Since both means are very similar, and MIX and MIO probe opposite polarisation directions, the heated-source emits unpolarised radiation. The oscillating feature below 120 GHz, found with MIO and MIX, is reproducible despite changing the experimental set up. A difference of about 8 K around the absorption line at 183 GHz is due to the changed concentration level of water vapour at different experimental days. (b) Relative uncertainties of $T_{HS,X}^{Rad}$ (dashed) and $T_{HS,O}^{Rad}$ (solid), respectively. The radiative temperatures are measured with the precision of less than 1% for a broad spectral domain. Below 70 GHz the results become more uncertain. In the vicinity of 557 GHz the water vapour absorption line elevates the uncertainty.

sessions. Furthermore, these two sessions are combined to compute $T_{HS,X}^{Rad}$ (see Fig. 10(a)) and its relative uncertainty (see Fig. 10(b)) to enter the derivation of the calibration factors for MIX. The relative uncertainty is below 1% for the spectral domain from 80 to 700 GHz except the region around the absorption line at 557 GHz. Below 80 GHz the uncertainty increases to about 30% at 30 GHz.

The oscillating feature present below 120 GHz is reproducible for each session. Changing the experimental procedure and conditions could not eliminate the oscillations.

2. Comparison of results using MIO and MIX

The radiative temperature $T_{HS,O}^{Rad}$ (see Fig. 10(a)) and its relative uncertainty (see Fig. 10(b)) relying on measurements with MIO, and, therefore, independent of MIX, is in very good agreement with $T_{HS,X}^{Rad}$ and its relative uncertainty. With this finding, and since MIX and MIO are sensitive to perpendicular polarisation directions, it is concluded that the heated-source emits an unpolarised spectrum.

As for $T_{HS,X}^{Rad}$ the oscillating feature is found below 120 GHz as well.

There is a systematic deviation between $T_{HS,O}^{Rad}$ and $T_{HS,X}^{Rad}$ of about 8 K around the water vapour absorption line at 183 GHz. This is probably caused by performing the measurements at different experimental days with

varying water vapour concentrations.

E. Absolute calibration: in-vessel task

While during the two MIX sessions 272 ($D \approx 33$ cm) and 134 ($D \approx 22$ cm) individual difference interferograms ΔV have been acquired, for the single MIO session 184 individuals are obtained. Having the background removed, individual phases and difference spectra ΔS are evaluated as described in Section IV B. For each session the mean for ΔS and its standard deviation of the mean are evaluated. The calibration factors follow from the definitions (22) and (24) using the radiative temperature $T_{HS,X}^{Rad}$ (or $T_{HS,O}^{Rad}$) of the heated-source (see section IV D and Fig. 10(a)) and the mean temperature T_{IS} of the intermediate-source (see Table II). The relative uncertainty in the calibration factors is evaluated using Gaussian error propagation for the quantities ΔS, $T_{HS,X}^{Rad}$ (or $T_{HS,O}^{Rad}$) and T_{IS}.

1. MIX

The two session means of ΔV are shown in Fig. 11 (a) close to the spatial origin. For both sessions the noise level reduction by the coherent averaging reveals small features for large optical path differences. The noise level for an individual ΔV accounts for 130 μV (=17.5 mV $\sqrt{2/35000}$), and for the sessions means one finds the level at 11 μV (=17.5 mV $\sqrt{2/(35000 \times 136)}$) and 16 μV,
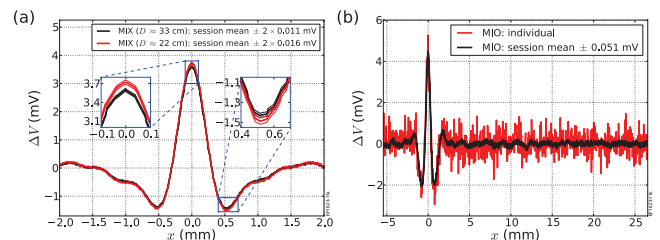

FIG. 11. In-vessel session means of difference interferograms ΔV dependent on optical path difference x determined with MIX and MIO diagnostics. For the two MIX sessions the distances D from the active surface of the heated-source to the in-vessel antenna and extension aperture have been $\approx$ 33 cm and $\approx$ 22 cm, respectively. The single MIO session was performed at $D \approx 33$ cm (no extension in place). (a) Session means of ΔV and associated two-sigma-uncertainty bands around ZPD position for MIX. Coherent averaging reduces the noise level in the spatial domain to 11 μV ($D \approx$ 33 cm) and 16 μV ($D \approx$ 22 cm), respectively. Clearly, for $D \approx$ 22 cm more signal is detected. (b) ΔV, individual (red) and session mean with associated one-sigma-uncertainty band (black), for MIO. The noise level for an individual reads 494 μV, and the uncertainty of the mean is given by 51 μV. Small features in the mean remain for large optical path differences.
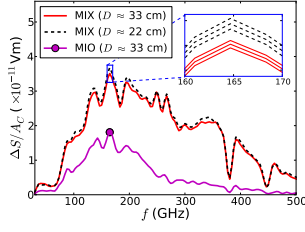
FIG. 12. In-vessel session means of difference spectra ΔS obtained with MIX (dashed and solid) and MIO (solid with dot) diagnostics. For scaling reasons ΔS divided by the amplification $A_C = 10^{4.5}$ and $10^{5.1}$ for MIX and MIO, respectively. D labels the distance from the active surface of the heated-source to the in-vessel antenna/extension aperture. Only for $D \approx 22$ cm the antenna extension was in place, and for this distance ΔS is larger in magnitude than for $D \approx 33$ cm. This increase is well above the two-sigma uncertainty of the measurement shown in the sub figure.

respectively. Hence, for the maximum signal at the ZPD position the SNR could be improved from approximately 1:30 to 1:330 with the coherent averaging technique.

For the second session the mean ΔV shows an increase of about 110 μV in amplitude in the vicinity of the origin when compared to the one for the first session. The signal difference exceeds the uncertainties determined.

The mean ΔS for both session have finite contributions in the spectral domain from 30 to 500 GHz, at least (see Fig. 12). Both have a maximum of about 3.6×10^{-11} Vm around 165 GHz, and ΔS approaches zero for low and high frequencies. The spatial uncertainty of an individual ΔV translates to the spectral uncertainty of about 2.4×10^{-12} Vm for an individual ΔS. Hence, the uncertainty of ΔS is close to 1.5 $\times 10^{-13}$ Vm for $D \approx 33$ cm and 2.1 $\times 10^{-13}$ Vm for $D \approx 22$ cm (see zoomed region in Fig. 12). Because the means are determined well enough, and ΔS for $D \approx 22$ exceeds almost everywhere its counterpart by several percent, a systematic increase is evident.

The calibration factors $C_{T,X}^{2015,\,33\,\mathrm{cm}}$ and $C_{T,X}^{2015,\,22\,\mathrm{cm}}$ on temperature scale and $C_{f,X}^{2015,\,33\,\mathrm{cm}}$ and $C_{f,X}^{2015,\,22\,\mathrm{cm}}$ on intensity scale are presented in Fig. 13(a) and (b). Quantitatively, $C_{T,X}^{2015,\,22\,\mathrm{cm}}$ is slightly larger than $C_{T,X}^{2015,\,33\,\mathrm{cm}}$ (for further discussion see Sec. IV E 3). For both sessions the relative uncertainties are at the level of 1% in the spectral domain 120–300 GHz (see Fig. 13(c)). The relative uncertainties below 100 GHz increase to about 10% at 60 GHz and to 50% at 30 GHz for both sessions.

The ratio of the means $C_{T,X}^{2015,\,22\,\mathrm{cm}}/C_{T,X}^{2015,\,33\,\mathrm{cm}}$ and its uncertainty are shown in Fig. 13(d). For the spectral domain from 100 to 300 GHz the average ratio is about 1.05 meaning $C_{T,X}^{2015,\,22\,\mathrm{cm}}$ is larger than $C_{T,X}^{2015,\,33\,\mathrm{cm}}$ by 5%. This increase exceeds the uncertainties, and, hence, for having the antenna extension in place the diagnostic response is higher.

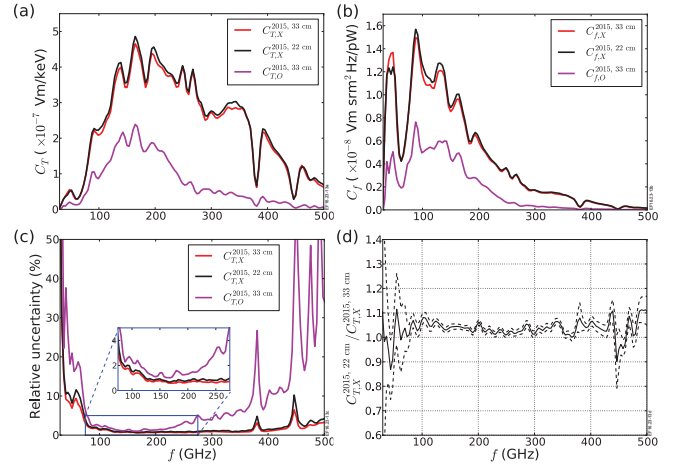The calibration factors $C_{T,X}^{2015,\,33\,\mathrm{cm}}$ are compared with

FIG. 13. Results of in-vessel absolute calibration of interferometers MIX and MIO for distances $D \approx 33$ and 22 cm (extension in place) in 2015. Uncertainties are evaluated with Gaussian error propagation. (a) Calibration factors $C_{T,X}^{2015,\,33\,\mathrm{cm}}$ (red) and $C_{T,X}^{2015,\,22\,\mathrm{cm}}$ (black) for MIX and $C_{T,O}^{2015,\,33\,\mathrm{cm}}$ (magenta) for MIO. For MIX the diagnostic response is higher for $D \approx 22$ cm. Due to higher attenuation by the transmission line (see Fig. 14(b)), MIO is less sensitive than MIX. (b) Calibration factors $C_{f,X}^{2015,\,33\,\mathrm{cm}}$ (red) and $C_{f,X}^{2015,\,22\,\mathrm{cm}}$ (black) for MIX and $C_{f,O}^{2015,\,33\,\mathrm{cm}}$ (magenta) for MIO on intensity scale. (c) Relative uncertainties of calibration factors. $C_{T,X}^{2015,\,33\,\mathrm{cm}}$ and $C_{T,X}^{2015,\,22\,\mathrm{cm}}$ are determined with better certainty than $C_{T,O}^{2015,\,33\,\mathrm{cm}}$, especially below 100 GHz and above 200 GHz. (d) Ratio (solid) of calibration factors for MIX with uncertainties (dashed). The sensitivity for $D \approx 22$ cm is significantly higher for the spectral domain 100–350 GHz, and the average increase is about 5%.

$C_{T,X}^{2010,\,33\,\mathrm{cm}}$ which capture the calibration from 2010 (see Ref.[12]) and are determined for the same separation distance D. The ratio $C_{T,X}^{2010,\,33\,\mathrm{cm}}/C_{T,X}^{2015,\,33\,\mathrm{cm}}$ reveals the relative change in the calibration over the years (see Fig. 14(a)). The diagnostic has become slightly more sensitive in the range 100–200 GHz and slightly less sensitive from 200 to 300 GHz. Furthermore, at water vapour absorption lines the change can be as high as 40%.

Fig. 14(b) shows the attenuation of the transmission line, evaluated by $10 \times \log_{10}(C_{T,X}^{2015,\,33\,\mathrm{cm}}/C_{T,X}^{BE,2015})$. The attenuation increases almost linear from -9 dB at 50 GHz to -21 dB at 500 GHz with some deviations, especially when dips are present around absorption lines of water vapour and oxygen.

2. MIO

One individual difference interferogram and the session mean for ΔV are shown in Fig. 11(b). The session mean shows remaining features above the noise level of 51 μV ($= 16.4$ mV $\sqrt{2/(35000 \times 92)} \times 10^{5.1-4.5}$) even for larger
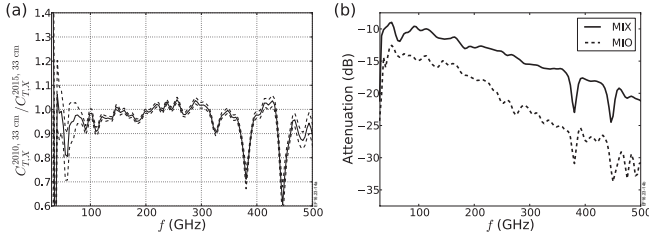
FIG. 14. (a) Ratio of calibration factors $C_{T,X}^{2010,\,33\,\text{cm}}/C_{T,X}^{2015,\,33\,\text{cm}}$, mean (solid) and uncertainty (dashed), as determined in 2010 and 2015 for interferometer MIX having heated-source placed 33 cm away from diagnostic antenna aperture. Since the ratio remains close to one in the spectral domain 100–300 GHz, the sensitivity has changed little. (b) Attenuation of transmission lines for interferometers MIX (solid) and MIO (dashed). Despite the similar geometry of the transmission lines (same antenna geometry, mainly S band waveguide with 12 mitre bends, length of about 40 m / 38 m for MIX / MIO), the attenuation in normal mode configuration (MIO) is larger than the one in tall mode configuration (MIX).

optical path differences. For the individual measurement the noise level is at 494 μV. Hence, for the maximum at the ZPD position the SNR elevates from roughly 1:9 to 1:85, which is about a factor of four smaller when related to the quantity for MIX.

The session mean ΔS is about a half of the one for the X-mode channel in the spectral domain from 30 to 160 GHz (see Fig. 12). For higher frequencies the amplitude is even more reduced. The uncertainty of an individual ΔS and the session mean read 2.3×10^{-12} Vm and 1.7×10^{-13} Vm, respectively.

As expected, the calibration factors $C_{T,O}^{2015,\,33\,\text{cm}}$ and $C_{f,O}^{2015,\,33\,\text{cm}}$ are smaller by at least a factor of two when compared with the results for MIX (see Fig. 13(a) and (b)). The calibration has the relative uncertainty of about 2.5% or less in the spectral domain 100–250 GHz. At 50 GHz and 360 GHz the relative uncertainty increases to 20% and 6%, respectively.

Despite having a very similar geometry for the transmission lines for both interferometers, the sensitivity for MIO is much smaller with respect to the one for MIX. This is explained by the larger attenuation of the MIO transmission line (see Fig. 14(b)). This attenuation accounts for -12.5 dB at 50 GHz and -32 dB at 500 GHz, which corresponds to the additional damping from -3.5 dB to -11 dB, when the transmission line (mainly S band waveguide) is used in normal mode.

3. Discussion of antenna pattern investigation

The two in-vessel sessions for MIX have been carried out during eight days and were separated by 34 hours. It is not expected that temporal variations of any kind affect the results such that the ratio $C_{T,X}^{2015,\,22\,\text{cm}}/C_{T,X}^{2015,\,33\,\text{cm}}$

(see Fig. 13(d)) remains close to 1.05 for the broad spectral domain 100–350 GHz. Hence, the increase in the response of about 5% is believed to be caused by having the extension in place. However, the influence of the extension on the in-vessel antenna pattern and, thus, the sensitivity has not been characterised in 2015. In order to do so, a third session, for which the heated-source is placed at 33 cm away from the extension, would be mandatory. Because this session is not available until the next calibration period, $C_{T,X}^{2015,\,33\,\text{cm}}$ and $C_{T,O}^{2015,\,33\,\text{cm}}$ are considered as the best estimates for the diagnostic sensitivities. Nevertheless, the systematic difference in the results is taken into account by the uncertainty estimation of the calibration (see Section IV E 5). This allows the test of any scientific hypothesis with respect to the calibration uncertainties.

4. Corrected calibration factors

Due to the change from re-chargeable batteries with the bias voltage of $V_{Bias} = 10$ V to long-life batteries with $V_{Bias} = 7.2$ V, the detector sensitivity S_D and, thus, the back end sensitivity changed, and a correction is needed. After probing the back end sensitivity for both bias voltages, one finds the correction simply by the ratio $C_T^{BE,\,7.2\,\text{V}}/C_T^{BE,\,10\,\text{V}}$, which varies spectrally around 1.07 for MIX and 1.11 for MIO. Hence, the diagnostic sensitivities have risen. With the correction the final form of the calibration factors for plasma operation is given by

$$C_{f,X(O)}^{2015,\,33\,\text{cm},\,7.2\,\text{V}} = C_{f,X(O)}^{2015,\,33\,\text{cm},\,10\,\text{V}}\,\frac{C_{T,X(O)}^{BE,\,7.2\,\text{V}}}{C_{T,X(O)}^{BE,\,10\,\text{V}}} \qquad (26)$$

and shown in Fig. 15(a). The uncertainty of the ratio enters in the uncertainty estimation described in the following subsection.

5. Revised Uncertainties

The uncertainty in the calibration as shown in Fig. 13(c) estimates the statistical confidence in the results during the corresponding calibration session. However, other sources of uncertainties have been identified: the back end sensitivity (see Section IV C 3), the issue about filling the in-vessel antenna pattern with the heated-source (see Section IV E 1), the change in the in-vessel calibration throughout years for comparable set up (see Section IV E 1), and the correction factors for using the long-life batteries (see Section IV E 4). For MIX and MIO those uncertainties will be estimated with Gaussian error propagation by

$$\sigma_{f,X(O)} = C_{f,X(O)}^{2015,\,33\,\text{cm},\,7.2\,\text{V}} \times \left[(r_{X(O)}^{10\,\text{V}\to7.2\,\text{V}})^2 + \right.$$
$$+ (r_{X(O)}^{2015,\,33\,\text{cm}})^2 + (r_X^{BE,\,2015})^2 +$$

the electron temperature profile, is the cutoff for waves in X- and O-mode polarisation caused by the plasma. A wave is evanescent, when it suffers the cutoff, and, hence, the detectable power vanishes or is massively reduced in amplitude. The relevant cutoff conditions are given below for the cold-plasma approximation and wave propagation perpendicular to the magnetic field as presented in Ref.[19].

For the O-mode wave with the frequency f a cutoff occurs when the relation $f \leq \omega_{pe}/(2\pi)$ is fulfilled, and the plasma frequency $\omega_{pe} = \sqrt{n_e e^2/(m_e \epsilon_0)}$ depends on the electron density n_e, the electron charge e and rest mass m_{e0}, and the dielectric constant ϵ_0. For example, the wave with $f = 80$ GHz is evanescent in the plasma medium where $n_e \geq 8 \times 10^{19}$ m^{-3}. Since n_e can be larger than 10^{20} m^{-3} for a JET plasma, this cutoff for the O-mode is a regular feature for the first harmonic range (O1), especially for the lower frequencies.

The cutoff features for the X-mode are more complicated. The relevant cutoff appears when the frequency f relates to the hybrid frequency $\omega_H = \sqrt{\Omega_{ce}^2 + \omega_{pe}^2}$ and the right-hand cutoff frequency $\omega_R = \Omega_{ce}\left(1 + \sqrt{1 + 4\omega_{pe}^2/\Omega_{ce}^2}\right)/2$ like $\omega_H < 2\pi f < \omega_R$. Both sides of the relation have a dependency on the electron cyclotron frequency $f_{ce} = \Omega_{ce}/(2\pi) = |\vec{B}|e/(2\pi m_e)$, and, thus, on the magnitude of the magnetic field $|\vec{B}|$. For JET conditions this relation implies that waves in X-mode polarisation for the first harmonic range can propagate inside the plasma towards the low-magnetic field side, where the diagnostic antennae are located. However, towards the plasma edge the density becomes small, and, thus, the cutoff condition is met for a wide frequency range. Hence, the entire first harmonic range (X1) experiences the cutoff. For lowered magnetic field strength and sufficiently high density the second harmonic range is affected as well.

2. Calibrated spectra

For each interferogram V' acquired with MIX and MIO the background is obtained and removed, the ZPD position is determined, and the phase and the spectrum S are evaluated (see Section IV B, Figs. 5(c)-(f) and Figs. 7(c) and (d)). Using the amplification A_P for plasma operation the calibrated spectrum in terms of radiative temperature follows from $T^{Rad} = S/(2A_P C_T)$ similar to equation (25). The corresponding uncertainty can be estimated by

$$\left(\frac{\sigma^{Rad}}{T^{Rad}}\right)^2 = \left[\left(\frac{\sigma_S}{S}\right)^2 + \left(\frac{\sigma_{C_T}}{C_T}\right)^2\right]. \quad (30)$$

While the second term in the above equation is at hand (see Fig. 15(b)), the first term is determined numerically as follows.

Since the interferogram is sampled spatially well enough at $\Delta x = 40$ μm ($f_{Max} = 3747$ GHz), V' is decomposed into four sub interferograms, so that $\Delta x = 160$ μm ($f_{Max} = 937$ GHz). For each of the four the entire processing is repeated to get four independent samples of the spectrum from which the standard deviation of the mean σ_S is evaluated.

For the three cases (see Table III) T_X^{Rad} and T_O^{Rad} with uncertainties are shown in Fig. 16 (a), (c) and (d) in the spectral range from 50 to 350 GHz covering the first three harmonic domains, at least. In general, for each harmonic range the radiative temperature is finite, even for the X1 domain, and the first and second harmonic ranges are well separated. The peak of the nth harmonic range follows the central magnetic field B_{Vac} multiplied with $n \times 28$ GHz/T. While in the spectral domains of O1 and X2 the peak heights are comparable for the small and intermediate n_e cases, the high n_e case shows a decrease of T_O^{Rad} with respect to T_X^{Rad}. This reduction is caused by the appearing cutoff which affects the lower frequencies in the spectral domain of O1. The radiative temperature for O2 approaches the one for X2 as the density increases, and, thus, the optical thickness must increase. For the
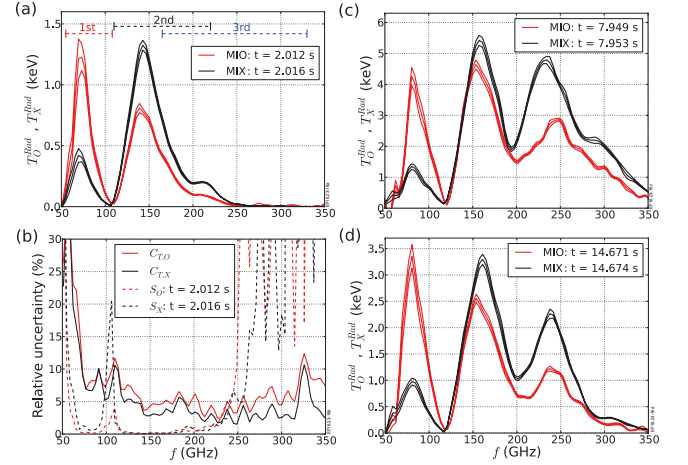
FIG. 16. Calibrated spectra T_X^{Rad} and T_O^{Rad} (in terms of radiative temperature) with uncertainties (one-σ) for three cases (before, during and after main heating phase, see Table III) of JET pulse 89074. At least three harmonic ranges can be seen. T_X^{Rad} for the second harmonic range and T_O^{Rad} for the first harmonic range are at similar levels, as long as there is no cutoff (see (c)). Theoretically, T_X^{Rad} for the 1st harmonic domain should be strongly damped due to cutoff, but a considerable peak is evident caused by multi-reflections at the inner JET wall and at the cutoff layer in the plasma. The calibration and the interferogram processing enter the uncertainties. (a) Case 1 (low n_e and T_e). The first three harmonic ranges are indicated (dashed). (b) Relative uncertainty for calibrated spectra presented in (a). The calibration uncertainty is of leading order as long as the radiative temperature is above 0.2 keV. (c) Case 2 (high n_e and T_e). Cutoff affects T_O^{Rad} below 75 GHz. (d) Case 3 (intermediate n_e and T_e).

third harmonic range, for which the plasma is optically thin, T_O^{Rad} and T_X^{Rad} increase with n_e and T_e.

Since the SNR is very large in the spectral and spatial domains, the uncertainties on T_X^{Rad} and T_O^{Rad} are given by the calibration uncertainties (for case 1 see Fig. 16(b)) for spectral domains where the radiative temperature exceeds about 0.2 keV.

3. ECE spectra

The calibrated spectra T_X^{Rad} and T_O^{Rad}, determined with MIX and MIO, are different from the pure ECE spectra T_{PX}^{Rad} and T_{PO}^{Rad} incident on each first polariser (see Fig. 1). The orientation of this polariser, while being spatially fixed, is rotated by an angle β with respect to the polarisation directions for X- and O-mode which depend on the magnetic field direction at the plasma edge. Hence, finite fractions of T_{PX}^{Rad} and T_{PO}^{Rad} are transmitted by the polariser and probed accordingly. Defining $\sin \beta = B_z/\sqrt{B_z^2 + B_{Tor}^2}$, where B_z and B_{Tor} abbreviate the magnitudes of the magnetic field components in z and toroidal directions at the crossing of the vacuum line of sight with the last closed flux surface, one finds with Malus' law that MIX (MIO) actually probes

$$T_{X(O)}^{Rad} = \cos^2(\beta)T_{PX(PO)}^{Rad} + \sin^2(\beta)T_{PO(PX)}^{Rad}. \quad (31)$$

Thereby, the right-hand side is usually not accessible due to the diagnostic principle. Nevertheless, an estimation of this effect can be deduced. By rearranging equation
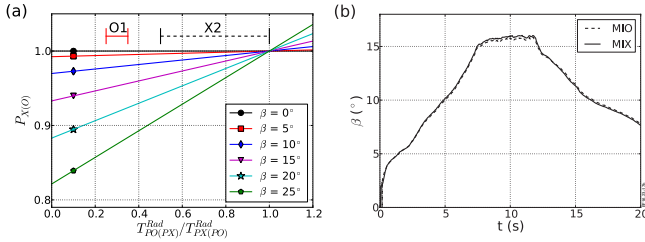

FIG. 17. (a) Pureness $P_{X(O)}$ of probed spectra dependent on angle β and ratio of pure ECE spectra $T_{PO(PX)}^{Rad}/T_{PX(PO)}^{Rad}$ in X- and O-mode polarisation incident on in-vessel antenna aperture. Finite β increases/reduces the pureness for spectral domains, for which the pure spectra are unequal. The pureness is different for the domains of O1 and of X2 for JET conditions, since the X1 domain is affected by the cutoff at the plasma edge. The pureness changes throughout a JET pulse due to varying β (see (b)) and electron density which changes the optical thickness for the O2 domain. (b) Angle β for diagnostics MIX and MIO for JET pulse 89074. The angle is evaluated from the magnetic field components in z and toroidal direction via $\sin \beta = |B_z|/\sqrt{B_z^2 + B_{Tor}^2}$ where the diagnostic vacuum line of sight crosses the last closed flux surface. During the pulse β increases up to about 16° and evolves similarly for MIX and MIO.

(31) the pureness

$$P_{X(O)} = \frac{T_{X(O)}^{Rad}}{T_{PX(PO)}^{Rad}} = 1 + \sin^2(\beta)\left(\frac{T_{PO(PX)}^{Rad}}{T_{PX(PO)}^{Rad}} - 1\right) (32)$$

is introduced which reveals that the probed spectra $T_{X(O)}^{Rad}$ can be enhanced/decreased with respect to the ECE spectra $T_{PX(PO)}^{Rad}$. For the domains O1 and X2, for which the plasma is optically thick, the pureness is generally smaller than one (for JET conditions see Fig. 17(a)), meaning that $T_{X(O)}^{Rad}$ is decreased with respect to $T_{PX(PO)}^{Rad}$. This is caused by ECE spectra in orthogonal polarisation directions which are not at the same level, and, thus, the ratio $T_{PO(PX)}^{Rad}/T_{PX(PO)}^{Rad}$ is smaller than unity for most cases. More precisely, at JET for the 1st harmonic domain $T_{PX}^{Rad}/T_{PO}^{Rad} \approx 0.3$ holds in general (see Section IV F 5), and for the second harmonic range the ratio $T_{PO}^{Rad}/T_{PX}^{Rad}$ takes values from 0.5 (small n_e) to 1 (high n_e) according to the optical thickness for the O-mode. Furthermore, since β depends via B_z on the plasma current I_P, at the plasma breakdown β vanishes and rises to about 15–20° for I_P of the order of some MA (see for JET pulse 89074 Fig. 17(b)). Hence, for example, if $\beta = 15°$ the pureness is at the level of 0.95 in the O1 domain, and if n_e (or optical thickness) is at a value, so that $T_{PO}^{Rad}/T_{PX}^{Rad} = 0.75$, the pureness reads about 0.98 in the X2 domain. These pureness values seem to be good estimates for most plasma parameter ranges at JET, excluding cutoff domains.

The ECE spectra can be accessed directly, when the plasma centre is located in the middle of the diagnostic vacuum lines of sight for MIX and MIO, and, therefore, the plasma and the flux surface geometry are probed similarly by the diagnostics. Furthermore, the angle β is alike for both diagnostics (see Fig. 17(b)). Starting from equation (31) one obtains

$$\begin{pmatrix} \cos^2\beta & \sin^2\beta \\ \sin^2\beta & \cos^2\beta \end{pmatrix}\begin{pmatrix} T_{PX}^{Rad} \\ T_{PO}^{Rad} \end{pmatrix} = \begin{pmatrix} T_X^{Rad} \\ T_O^{Rad} \end{pmatrix} \quad (33)$$

which is inverted to

$$\begin{pmatrix} T_{PX}^{Rad} \\ T_{PO}^{Rad} \end{pmatrix} = \quad (34)$$

$$= \begin{pmatrix} \frac{\cos^2\beta}{\cos^4\beta - \sin^4\beta} & -\frac{\sin^2\beta}{\cos^4\beta - \sin^4\beta} \\ -\frac{\sin^2\beta}{\cos^4\beta - \sin^4\beta} & \frac{\cos^2\beta}{\cos^4\beta - \sin^4\beta} \end{pmatrix}\begin{pmatrix} T_X^{Rad} \\ T_O^{Rad} \end{pmatrix}.$$

The circumstances are met for the cases 1 ($\beta = 5.8°$) and 3 ($\beta = 11.8°$) to apply the above formula. The pureness, which follows, behaves differently for the first and second harmonic ranges (see Fig. 18(a) and (b)). While in the first harmonic range for both polarisations a plateau-like increase/decrease of some percentage is present even for small β, the pureness remains close to unity in the second harmonic range as the frequency and β become larger.
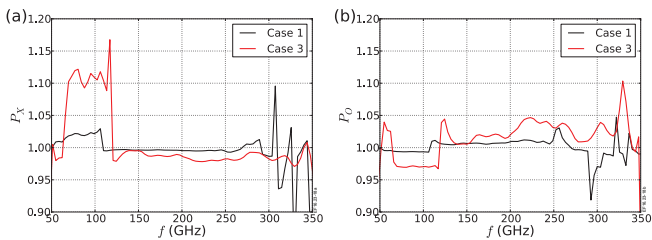
FIG. 18. Pureness $P_{X(O)}$ directly accessed for case 1 ($\beta = 5.8°$) and case 3 ($\beta = 11.8°$). While the pureness for both polarisations has a plateau-like deviation from unity even for small β in the first harmonic range (60–110 GHz), it ramps away from unity in the second harmonic range as frequency and β increase. (a) For X-mode. (b) For O-mode.

4. Temperature Profile

The electron temperature profile T_e is deduced with the cold-resonance method for the magnetic field configuration and the flux surface geometry given by the equilibrium reconstruction tool EFIT[20]. Though, this EFIT version (internal JET abbreviation EHPB) uses the more accurate optical fibre measurement to obtain the current flowing through the toroidal field coils[21].

The cold-resonance method assumes infinite optical thickness ($T_e = T^{Rad}$) for the spectral ranges O1 and X2 under consideration for JET conditions and omits refraction effects like the deviation from the vacuum line of sight and finite antenna pattern effects. The method connects the probing frequency f with the electron cyclotron frequency f_{ce} for a cold plasma and localises the emission via the magnitude $|\vec{B}|$ of the magnetic field along the vacuum line of sight R_{LOS}. For the n-th harmonic range the localisation follows from $f(R_{LOS}) = n f_{ce} = n|\vec{B}|(R_{LOS}) \times e/(2\pi m_{e0})$, whereat the overlap of the domains X2 and X3 is excluded and cutoff affected frequencies in the O1 domain need to be rejected. Furthermore, the mapping from the spatial domain to the flux surface label, here the normalised poloidal flux Ψ_N, is essential for drawing conclusions from the derived profile $T_e(\Psi_N)$. While the uncertainty of T_e is taken from the ECE spectrum directly, the uncertainty of Ψ_N is determined in terms of resolution as follows.

The processing of the interferogram applies the window function W_S which translates into the characteristic convolution in the spectral domain (see Section IV B 5 and Fig. 6(b)). This convolution states that the value, say the emission, of a spectral channel at a given frequency f corresponds actually to the weighted average in the range $f \pm 2.8$ GHz. By mapping those channel boundaries with the cold-resonance method, the resolution in Ψ_N is obtained.

For the three cases (see Table III) the profiles $T_e(\Psi_N)$ are determined (see Fig. 19(a)-(c)). While the cases 1 and 3 allow the use of the pure ECE spectra T_{PX}^{Rad} and T_{PO}^{Rad}, for case 2 the calibrated spectra T_X^{Rad} and T_O^{Rad}

are increased by 5% (O1) and 2% (X2) to correct for $\beta \approx 15°$ (see Section IV F 3 and Fig. 17). Since the gradient of B is small on the outboard side ($\Psi_N > 0$), the resolution is poor for $T_e(\Psi_N)$ when inferred from the O1 domain (see Fig. 19(a)). Hence, only the inboard part ($\Psi_N < 0$) is shown for the cases 2 and 3. Furthermore, the O1 domain, which is affected by the cutoff, is not shown for case 2. In general, the profile obtained from the X2 domain covers the region $\Psi_N > -0.2$ and overlaps nicely with the one for the O1 domain, which itself extends to the plasma edge on the inboard side. For the case 2, the resolution is left out for the sake of comparison with the temperature profile as deduced by the Thomson scattering diagnostic LIDAR[22,23]. The profiles probed with three independent diagnostics are mostly in good agreement. For the third case (intermediate n_e) the profiles are tested with respect to the constancy of the temperature on a given flux surface (see Fig. 19(d)). This reveals a loop-shape due to the systematic deviation, for example 0.5 keV at $\Psi_N = 0.4$, between inboard and outboard partial profiles. Note, any relativistic correction in the mapping procedure would increase the systematic difference. Since the width of loop seems to vanish for case 1 (low n_e, Ohmic heating) while being present for the cases 2 (high n_e) and 3, it cannot be explained with the optical thickness being much different for frequencies in the O1 and X2 domains. However, the calibrations for both interferometers could be systematically wrong. But this seems unlikely, because the inboard partial profiles determined for MIX and MIO overlap almost seamlessly in general. Causes which are linked to the equilibrium are more probable, if a Maxwellian velocity distribution function is assumed. The magnitude of the magnetic field along the line of sight could be too low, and/or the Shafranov shift for the flux surfaces could be underestimated.

5. Enhancement by multiple reflections

Theoretically, as explained in Section IV F 1 the cutoff layer, located somewhere inside the plasma on the outboard side, prevents the ECE spectrum T_{PX}^{Rad} in X-mode polarisation of the first harmonic range from leaving the plasma unhindered. In consequence of that, T_{PX}^{Rad} must be damped strongly or even vanish after passing through the cutoff layer. On the contrary, T_X^{Rad} measured has a considerable amplitude (see Fig. 16). This enhanced level can be explained by multiple reflections at the JET inner wall, causing polarisation-scrambling in addition, and subsequent to that at the cutoff layer.

As the O-mode propagates outside the plasma towards the low-magnetic field side, a direct coupling to the diagnostic antenna follows. The radiation, which misses the antenna, propagates further towards the wall at the outboard side of JET, where reflection and scrambling occur. The power returning in O-mode polarisation after the reflection at the wall is re-absorbed by the plasma.
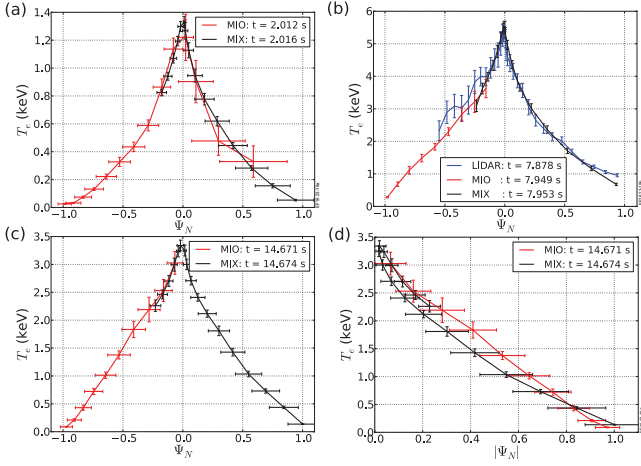
FIG. 19. Electron temperature profiles T_e dependent on normalised poloidal flux Ψ_N for three cases of JET pulse 89074 (see Table III). Starting from the O1 and X2 domains of the ECE spectra (case 1 and case 3) and of the calibrated spectra (case 2), the cold-resonance method translates the probing frequency f to Ψ_N using the equilibrium tool EFIT (JET version EHPB). While T_e inherits the uncertainties from the ECE spectra, the uncertainty (resolution) for Ψ_N is determined from the spectral resolution $\pm$ 2.8 GHz of the interferometers (see Section IV B 3 and Fig. 6(b)). While the profile, inferred from the X2 domain (black), covers the inboard side ($\Psi_N < 0$) only partly, the profile deduced for the O1 domain (red) extends to the plasma edge at $\Psi_N = -1$. Convincingly good overlap of both profiles is achieved. Since the resolution for the profile (O1 domain) is generally very poor on the outboard side, it is presented completely only for case 1. (a) Case 1 (low electron density n_e). (b). Case 2 (high n_e). Due to cutoff the profile determined with MIO is only available below $\Psi_N < -0.15$. The resolution is left out to ease the visual comparison with the profile probed independently by the Thomson scattering diagnostic LIDAR[22,23] (blue). Reasonably good agreement is achieved. (c) Case 3 (intermediate n_e). (d) Case 3 comparing inboard and outboard profile branches. Since the inboard branch is higher by some 100 eV, the profile determined does not preserve the temperature on a flux surface. The deviation in shape of a loop can be caused by the diagnostic calibrations, too low magnetic field strength and/or underestimated Shafranov shift in the flux surface geometry. Any relativistic correction would increase the width of the loop.

In contrast, the cutoff layer reflects the spectrum in X-mode polarisation present only due to the prior scrambling. Together with the O-mode spectrum, just emitted by the plasma, the X-mode spectrum propagates towards the first wall and the diagnostic antenna. This sequence comprising the emission in O-mode polarisation by the plasma, the reflection and scrambling at the wall, and the reflection of the returning radiation in X-mode polarisation at the cutoff layer while O-mode radiation is re-absorbed by the plasma, repeats itself. Summing the iterative contributions of this process and the direct coupling to the antenna gives the total power available at the diagnostic antenna.

In order to perform the summation, a common model is used which has two parameters, the reflection coefficient R and the polarisation-scrambling coefficient M. While R captures the fraction of the power reflected, M states how much power is transferred between the perpendicular polarisation directions. Both coefficients are assumed to be constant for the entire spectral domain, and a physical meaning is achieved only for values between 0 and 1. With the simple model one finds the expression

$$
\begin{pmatrix} T_{PX}^{Rad} \\ T_{PO}^{Rad} \end{pmatrix} = \sum_{k=0}^{\infty} (R_X W_P)^k \begin{pmatrix} 0 \\ T_{PO}^{Rad} \end{pmatrix} \qquad (35)
$$

with the matrices

$$
W_P = R \begin{pmatrix} (1-M) & M \\ M & (1-M) \end{pmatrix}, \qquad (36)
$$

describing the reflection and the polarisation-scrambling at the wall and

$$
R_X = \begin{pmatrix} 1 & 0 \\ 0 & 0 \end{pmatrix}, \qquad (37)
$$

for the total absorption of the returning radiation in O-mode polarisation by the plasma and the total reflection of radiation in X-mode polarisation by the cutoff layer. For $k = 0$ the direct contribution is obtained. After some algebra

$$
\begin{pmatrix} T_{PX}^{Rad} \\ T_{PO}^{Rad} \end{pmatrix} = T_{PO}^{Rad} \begin{pmatrix} \frac{RM}{1-(1-M)R} \\ 1 \end{pmatrix} \qquad (38)
$$

remains, where $\sum_{k=0}^{\infty} ((1-M)R)^k = 1/(1-(1-M)R)$ has been used. A unique solution does not exist. But by dividing both equations (38) the solution curve

$$
M = \frac{T_{PX/PO}}{1 - T_{PX/PO}} \frac{1-R}{R} \qquad (39)
$$

is found using the ratio $T_{PX/PO} = T_{PX}^{Rad}/T_{PO}^{Rad}$. Due to the $1/R$ dependency, if less/more power is reflected by the wall, then the polarisation-scrambling needs to be increased/reduced accordingly. Furthermore, as R approaches unity, M vanishes, while for the reasonable limit $M = 1$ a lower limit for the reflection coefficient $R = T_{PX/PO}$ is obtained.

For the cases 1 and 3 MIX and MIO probe the plasma similarly as described in Section IV F 3. Thus, $T_{PX/PO}$ is available, and this ratio takes values in the range 0.3 $\pm$ 0.05. For this range, a narrow band is formed in the R-M-plane which passes through a region found by a probabilistic approach (see Fig. 20). This probabilistic approach[24] models the wall properties in the same way as stated by equation (36). However, the ray-tracer SPECE is exploited to model the calibrated spectrum probed with MIX in the 2nd, 3rd and 4th harmonic
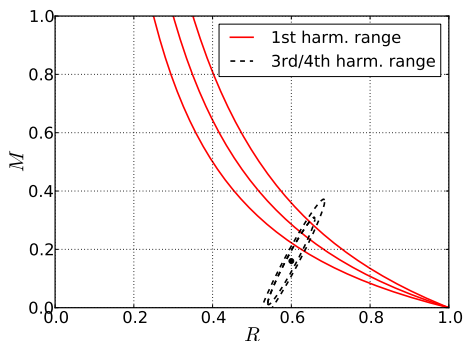
FIG. 20. Condition on polarisation-scrambling coefficient $M = \left[T_{PX/PO}/(1 - T_{PX/PO})\right](1 - R)/R$ (solid) dependent on reflectivity R of JET inner wall on outboard side to enhance spectrum in X1 domain. Having the ECE spectra T_{PX}^{Rad} in X-mode polarisation and T_{PO}^{Rad} in O-mode polarisation probed, the ratio $T_{PX/PO} = T_{PX}^{Rad}/T_{PO}^{Rad}$ determines the condition with the $1/R$ dependency. For the cases 1 and 3 (see Table III), $T_{PX/PO}$ takes values in the range 0.3 ± 0.05 which determines the minimum for R at the meaningful limit $M = 1$. The condition passes through the region of high confidence (black ellipses) around the most likely combination $R = 0.6$ and $M = 0.16$ (black dot) obtained with a probabilistic approach[24]. This alternative approach estimates R and M and their uncertainties and correlation from the calibrated spectrum probed by MIX in the third and fourth harmonic range. Hence, the wall properties for the JET inner wall on the inboard and outboard side are probed. Since the results rely on different spectral ranges but have an overlap, the simple model for the wall reflections is a good approximation.

ranges. Thus, the wall properties, expressed in probabilistic terms by the means $R = 0.6$ and $M = 0.16$, the uncertainties $\sigma_R = 0.05$ and $\sigma_M = 0.15$ and the correlation coefficient of 0.97, are determined for the first wall on the inboard and outboard side of JET. On the contrary, the results derived here take into account the first harmonic range and only the first wall on the outboard side. Since an overlapping region for both findings is present, the simple model for the wall properties is a good approximation, especially the assumption that R and M have no dependency on frequency.

V. CONCLUSIONS

The ECE diagnostic system at JET was upgraded with a second interferometer MIO being similar in construction as MIX. The calibration set up has been updated for both diagnostics. The main feature is the in-vessel antenna extension which could be fitted with MASCOT remotely controlled. This allowed the investigation of the antenna pattern with MIX.

The general principle of the analysis for calibration and plasma operation has been presented in detail. This includes the characterisation of the convolution inherent to Fourier spectroscopy diagnostics like MIX and MIO.

The interferometers have been calibrated absolutely and independently. MIX has a better sensitivity than MIO, since the latter diagnostic uses a similar transmission line (mainly S-band waveguide) in normal mode. To improve the sensitivity for MIO, the polarisation direction passing the first polariser needs to be rotated by 90 degrees, so that tall mode usage of the transmission line is obtained. Investigations are ongoing to achieve the rotation by an additional wire grid and a rooftop mirror located just behind the first polariser.

Several aspects of the diagnostic calibration have been investigated. The most important uncertainty (at least 5% in relative terms) arises from filling the in-vessel antenna pattern with the heated-source. However, this issue needs further investigation in the next JET shutdown. The influence of the antenna extension has to be characterised by scanning the separation distance from the heated-source to the extension aperture in the range 10–30 cm. Sufficient experimental time is already assigned. Since the antenna pattern issue is difficult to address in a running fusion experiment, it is recommended to determine the pattern for any in-vessel antenna including its transmission line for future ECE diagnostics prior to the final commissioning. Besides this aspect, a long-term study of the back end sensitivity has been carried out for MIX. A relative uncertainty of at least 1.5% could be found increased even further for spectral domains around atmospheric absorption lines. The lower limit for the total uncertainty (one-σ) for the absolute sensitivity is stated roughly by: 1% (for one calibration session), 2.5% (antenna pattern), 1.5% (change in back end sensitivity), 0–5% (change in total sensitivity over years).

The comparison of the central electron temperatures measured independently with LIDAR and MIX (with the 2015 calibration) reveals a good agreement. Hence, the calibration was considered acceptable and was applied from JET pulse 88001 onwards. MIO is operating from pulse 88089.

With MIX and MIO the ECE spectra in X- and O-mode polarisation are simultaneously probed at JET. The response of the different harmonic ranges can be studied with respect to the plasma parameters. Thereby, the cutoff for parts of the first harmonic range in O-mode polarisation is noticeable.

Having the ECE spectra probed in both polarisation directions, advanced analysis techniques[24] are enabled exploiting ECE ray-tracing tools like SPECE[14] and TRAVIS[25]. Since these tools rely on models which include for example the cyclotron emission and absorption by plasma electrons, antenna pattern effects, refraction effects and arbitrary velocity distribution functions for electrons, more information can be extracted from the ECE spectra. If the model predictions are in good agreement with the measured quantities for plasmas with a justified Maxwellian velocity distribution, then non-Maxwellian features could be identified in the ECE spectra for extreme plasma parameter ranges.

For suited electron density and magnetic field strength ranges, the first harmonic range in O-mode polarisation allows the derivation of the electron temperature profile on the inboard side of JET. The proof of principle relying on measurements with MIO has been presented. At the moment, that is the only way to probe the inboard and outboard temperature profile at JET. However, due to the cutoff and calibration uncertainties the magnetic field strength at the plasma centre should be at least 2.5 T for ECE measurements. For the representative example shown, the assumption, which is considered to be valid, that the electron temperature is preserved on a given flux surface, is violated. Most likely, this is caused by having wrongly captured the magnetic field strength and/or the flux surface geometry. Investigations are ongoing to constrain the equilibrium reconstruction, so that the deduced T_e is preserved on a flux surface.

The detected ECE spectrum in the X1 domain shows an enhanced level despite suffering from cutoff. To explain this feature a common model is used which takes into account polarisation-scrambling and multi-reflections between the first wall of JET on the outboard side and the cutoff layer inside the plasma. An analytical condition for M is obtained with a $1/R$ dependency for the reflection and the polarisation-scrambling coefficients R and M, respectively. This result agrees well with the finding of an alternative approach. Since both approaches probe the JET first wall differently and exploit mutual exclusive harmonic ranges of the ECE spectra, the simple model for the reflections at the wall seems to be a good approximation.

Spectral channels of the heterodyne radiometer diagnostic (fast temporal and better spectral/spatial resolution than the interferometers), which probe the first harmonic range in O-mode polarisation, will be routinely cross-calibrated with respect to MIO. Hence, the pedestal region on the inboard side of JET will become accessible, and a comparison with the pedestal on the outboard side will be possible.

VI. ACKNOWLEDGMENTS

[1] F. J. Stauffer, D. A. Boyd, R. C. Cutler, M. Diesso, M. P. Mc-Carthy, J. Montague, and R. Rocco, *Rev. Sci. Instrum.* 59, 2139 (1988).

[2] M. E. Austin, R. F. Ellis, J. L. Doane, and R. A. James, *Rev. Sci. Instrum.* 68, 480 (1997).

[3] A.E. Costley, *Fusion Sci. Technol.* 55, 1 (2009).

[4] D.H. Martin and E. Puplett, *Infrared Phys.* 10, 105 (1969).

[5] A. E. Costley, E. A. M. Baker, M. G. Kiff and G. F. Neill, *Proc. of 3rd Joint Workshop on Electron Cyclotron Emission and Electron Cyclotron Resonance Heating*, Madison, USA,1982, p. 1.

[6] E. A. M. Baker, D. V. Bartlett, D. J. Campbell, A. E. Costley, M. G. Kiff and G. F. Neill, *Proc. of 8th International Conference on Infrared and Millimeter Waves*, Miami, USA, 1983.

[7] A. E. Costley, E. A. M. Baker, D. V. Bartlett, D. J. Campbell, M. G. Kiff, S. E. Kissel, G. F. Neill and P. F. Roach, *Proc. of 5th Joint Workshop on Electron Cyclotron Emission and Electron Cyclotron Resonance Heating*, San Diego, California, USA, 1985, p. 18.

[8] A. E. Costley, E. A. M. Baker, D. V. Bartlett, D. J. Campbell, M. G. Kiff and G. F. Neill, *Proc. of 4th Joint Workshop on Electron Cyclotron Emission and Electron Cyclotron Resonance Heating*, Rome, Italy, 1984, p. 1.

[9] E. A. M. Baker, D. V. Bartlett, D. J. Campbell, A. E. Costley, D. J. Daly, A. Dellis, L. C. J. M. De Kock, and J. Fessey, *Proc. of 4th Joint Workshop on Electron Cyclotron Emission and Electron Cyclotron Resonance Heating*, Rome, Italy, 1984, p. 11.

[10] E. A. M. Baker, D. V. Bartlett, D. J. Campbell, A. E. Costley, A. E. Hubbard and D. G. Moss, *Proc. of 4th Joint Workshop on Electron Cyclotron Emission and Electron Cyclotron Resonance Heating*, Rome, Italy, 1984, p. 23.

[11] D. V. Bartlett, D. J. Campbell, A. E. Costley, S. Kissel, N. Lopes Cardozo, C. W. Gowers, S. Nowak, T. Oyevaar, N. A. Salmon and B. J. Tubbing, *Proc. of 6th Joint Workshop on Electron Cyclotron Emission and Electron Cyclotron Resonance Heating*, Oxford, UK, 1987, p. 137.

[12] S. Schmuck, J. Fessey, T. Gerbaud, B. Alper, M. N. A. Beurskens, E. de la Luna, A. Sirinelli, M. Zerbini, and JET-EFDA Contributors, *Rev. Sci. Instrum.* 83, 125101 (2012).

[13] L. Barrera, E. de la Luna, L. Figini, M. N. A. Beurskens, M. Brix, F. Castejón, P. C. de Vries, D. Farina, M. Kempenaars, P. Lomas, J. Mailloux, I. Nunes, E. R. Solano, and JET-EFDA Contributors, *Plasma Phys. Control. Fusion* 52, 085010 (2010).

[14] D. Farina, L. Figini, P. Platania, and C. Sozzi, *Proc. of BURNING PLASMA DIAGNOSTICS: An International Conference*, Varenna, Italy, 2007, edited by G. Gorini, F. P. Orsitto, E. Sindoni, M. Tardocchi, p. 128.

[15] E. de la Luna, J. Sánchez, V. Tribaldos, JET-EFDA contributors, G. Conway, W. Suttrop, J. Fessey, R. Prentice, C. Gowers, and J. M. Chareau, *Rev. Sci. Instrum.* 75, 3831 (2004).

[16] Tesselating Terahertz RAM radar absorbing material by Thomas Keating Ltd. See http://www.terahertz.co.uk for description and specifications.

[17] A. Loving, P. Allan, N. Sykes, S. Collins, and P. Murcutt, *Proc. of 10th International Symposium on Fusion Nuclear Technology*, Portland, USA, 2011.

[18] M. Bornatici, R. Cano, O. De Barbieri, and F. Engelmann, *Nucl. Fusion* 23 , 1153 (1983).

[19] I. H. Hutchinson, *Principles of Plasma Diagnostics Second Edition* (Cambridge University Press, New York, 2002) p. 173.

[20] L.L. Lao, J.R. Ferron, R.J. Groebner, W. Howl, H. S. John, E. J. Strait, and T. S. Taylor, *Nucl. Fusion* 30, 1035 (1990).

[21] R. Salmon, P. Smith, A. West, S. Shaw, D. Rendell and JET EFDA contributors, *Proc. of the 28th Symposium On Fusion Technology (SOFT-28)*, *Fusion Eng. Des.* 98–99, 1148 (2014).

[22] C. W. Gowers, B. W. Brown, H. Fajemirokun, P. Nielsen, Y. Nizienko, and B. Schunke, *Rev. Sci. Instrum.* 66, 471 (1995).

[23] H. Salzmann, J. Bundgaard, A. Gadd, C. Gowers, K. B. Hansen, K. Hirsch, P. Nielsen, K. Reed, C. Schroedter, and K. Weisberg, *Rev. Sci. Instrum.* 59, 1451 (1988).

[24] S. Schmuck, J. Svensson, L. Figini, T. Jonsson, J. Fessey, L. Meneses, J.E. Boom and JET EFDA contributors, *Proc. of 41th EPS Conference on Plasma Physics*, Berlin, Germany, 2014.

[25] N. B. Marushchenko, Y. Turkin, and H. Maassberg, *Comput.*

Phys. Commun. 185, 1 (2014).